POLYTECHNIQUE MONTRÉAL
affiliée à l'Université de Montréal

Simulation Of The Vibratory Peening Process

LUCAS DE LA TORRE
Département de génie mécanique

Mémoire présenté en vue de l'obtention du diplôme de *Maîtrise ès sciences appliquées*
Génie mécanique

Octobre 2022

POLYTECHNIQUE MONTRÉAL
affiliée à l'Université de Montréal

Ce mémoire intitulé :

Simulation Of The Vibratory Peening Process

présenté par **Lucas DE LA TORRE**
en vue de l'obtention du diplôme de *Maîtrise ès sciences appliquées*
a été dûment accepté par le jury d'examen constitué de :

Sylvain TURENNE, président
Martin LÉVESQUE, membre et directeur de recherche
Benoit CHANGEUX, membre et codirecteur de recherche
Bruno BLAIS, membre

DEDICATION

To my lovely mother,
To my brave father,
To my marvellous brother,
To my caring grandparents,
To my wonderful wife.....

ACKNOWLEDGEMENTS

I would like to express my sincere thanks to Prof. Martin Lévesque, my director, who allowed me to complete this master thesis under his supervision. His advice was invaluable in guiding me in my research.

I am also very grateful for the work done by Dr. Hongyan Miao, who helped me to improve my writing and presentation skills considerably. She helped me write this master's thesis and allowed this project to be ordered and completed.

I also would like to thank Prof. Sylvain Turenne for giving his advice during our discussions throughout this project.

I would also like to thank the industrial members of the project, Dr. Jawad Baddredine and Dr. Benoit Changeux from Safran who also gave me valuable advice in my simulations and more generally in the supervision of the project. Many thanks to the company Safran who allowed this project to be carried out by their funding.

I would also like to thank the Natural Science and Engineering Research Council of Canada (NSERC) who also funded the project.

I would also like to acknowledge the contribution of Khouloud Chouchane, Maxime Paques and Abouthaina Saadallah for their help and support throughout this project. Thanks also to the members of the LM2 laboratory for their assistance.

Finally, I would like to thank my family who encouraged me to go to Canada to pursue this project.

RÉSUMÉ

Le grenaillage vibratoire est un procédé de finition qui combine deux procédés en un. Il a le même effet que le grenaillage conventionnel qui augmente la durée de vie en fatigue en introduisant des contraintes résiduelles de compression tout en polissant la pièce traitée, ce qui est généralement fait par tribofinition. Ce procédé est également censé améliorer la productivité industrielle puisqu'il combine le grenaillage de précontrainte et la tribofinition en un seul procédé.

Cette étude fait partie d'un projet plus général qui vise à expliquer les avantages des technologies avancées de traitement de surface sur les matériaux aérospatiaux. Polytechnique Montréal a collaboré avec Safran France et le Centre technologique en aérospatiale (CTA). Ce travail se concentre sur la réalisation d'une étude préliminaire de simulations par éléments discrets afin d'évaluer les champs de vitesse à l'intérieur de la machine de grenaillage vibratoire pendant son fonctionnement. Il comprend également une étude expérimentale permettant d'instrumenter la machine de grenaillage vibratoire afin de déterminer le mouvement 3D de la machine de grenaillage vibratoire.

La revue de la littérature a révélé que l'amplitude et la fréquence de la machine de grenaillage vibratoire étaient les paramètres les plus pertinents pour caractériser les effets du grenaillage vibratoire. La première partie de l'introduction présente le processus de grenaillage vibratoire et les paramètres qui caractérisent le processus tels que la couverture et l'intensité Almen. Les études ont montré que le grenaillage conventionnel et le grenaillage vibratoire peuvent atteindre une gamme d'intensité Almen de 0.12 mmA à 0.25 mmA. La deuxième partie se concentre sur les moyens de contrôler une machine de grenaillage vibratoire. La modélisation cinématique de la machine montre que le mouvement d'une machine de grenaillage vibratoire est vertical. Cette partie montre également les technologies courantes qui permettent de mesurer les vibrations à basse fréquence. La troisième partie de la revue de la littérature a présenté les méthodes de modélisation de l'écoulement granulaire. Elle a montré que la méthode des éléments discrets est la plus pertinente pour mesurer les champs de vitesse à l'intérieur d'une machine de grenaillage vibratoire. Les études réalisées avec la méthode des éléments discrets ont montré que les forces normales entre la grenaille et la pièce contribuent à l'effet de martelage tandis que les forces tangentielles contribuent à l'effet de polissage.

Les expériences ont montré que le grenaillage vibratoire a principalement des modes de vibration verticaux tandis que les modes de vibration rotatifs et horizontaux peuvent être négligés. L'amplitude de la machine de grenaillage vibratoire aux fréquences d'arbre imposées

de 17.5 Hz à 30 Hz varie de 1.7 mm à 2.6 mm. Pour des fréquences d'arbre spécifiques, le deuxième mode de vibration influence les champs de déplacement et de vitesse des grenailles à l'intérieur de la machine de grenaillage vibratoire. Il s'agit d'un mode de vibration de basse fréquence à 3 Hz pour les fréquences d'arbre de 22.5 Hz et 30 Hz. L'amplitude est respectivement de 5.3 mm et 8.5 mm à 22.5 Hz et 30 Hz. Les simulations basées sur le mouvement mesuré de la machine de grenaillage vibratoire ont montré que la vitesse d'impact normale de la grenaille sur la pièce varie linéairement avec la fréquence de l'arbre de la machine de grenaillage vibratoire. La vitesse d'impact atteint 0.6 m/s à 17.5 Hz et 0.95 m/s à 30 Hz. De plus, une corrélation linéaire a été trouvée entre l'intensité Almen et la vitesse d'impact. Enfin, cette étude préliminaire a permis de conclure que la méthode des éléments discrets était appropriée pour avoir une meilleure compréhension du processus de grenaillage vibratoire et guider les prochaines recherches sur l'interaction entre les grenailles et la pièce avec le processus de grenaillage vibratoire.

ABSTRACT

Vibratory peening is a finishing process that combines two processes in one. It has the same effect as shot peening that increases fatigue life by inducing compressive residual stresses while polishing the treated part, which is usually done by vibratory finishing. This process is also believed to improve the industrial productivity since it combines the shot peening and the vibratory finishing processes into one single process.

This study is part of a more general project that aims to explain the befenits of advanced surface treatment technologies on aerospace materials. Polytechnique Montréal collaborated with Safran France and Centre Technologique en Aérospatiale (CTA). This work concentrates on realizing a preliminary study of discrete elements simulations to assess velocity fields inside the vibratory peening machine during operation. It also involves an experimental study to intrument the vibratory peening machine to determine its 3D motion.

The literature review reveals that the amplitude and the frequency of the vibratory peening machine were the most relevant parameters to characterize the effects of the process. The first part of the literature survey presents the vibratory peening process and the parameters that characterize it such as coverage and Almen intensity. The studies show that both shot peening and vibratory peening can reach a range of Almen intensities of 0.12 mmA to 0.25 mmA. The second part focuses on the ways of monitoring a vibratory peening machine. The kinematic modelling of the machine shows that the motion of a vibratory peening machine is vertical. This part also shows the common technologies able to measure vibrations at low frequencies. The third part of the literature review presents the ways of modelling granular flow. It shows that the discrete element method is the most relevant method to predict velocity fields inside a vibratory peening machine. The studies produced with the discrete element method show that normal forces between shot and the workpiece contributed to the peening effect while tangential forces contributed to the polishing effect.

The experiments show that our vibratory peening machine has mainly vertical modes of vibrations. The amplitude of the vibratory peening machine at imposed shaft frequencies ranging from 17.5 Hz to 30 Hz varies from 1.7 mm to 2.6 mm. For specific shaft frequencies, second mode of vibration influences the displacement and velocity fields of media inside the vibratory peening machine. The second mode of vibration is a typical frequency of 3 Hz for 22.5 Hz and 30 Hz shaft frequencies. The amplitude is respectively of 5.3 mm and 8.5 mm at 22.5 Hz and 30 Hz. The simulations based on the measured motion of the vibratory peening machine show that the normal impact velocity of shot on the workpiece varies linearly with

the shaft frequency of the vibratory peening machine. The impact velocity reaches 0.6 m/s at 17.5 Hz and 0.95 m/s at 30 Hz. Moreover, a linear correlation has been found between Almen intensity and impact velocity. Finally, this preliminary study permits to conclude that the discrete element method was appropriate to have a better understanding of the vibratory peening process and guide the next research about the interaction between media and workpiece with the vibratory peening process.

TABLE OF CONTENTS

LIST OF TABLES

LIST OF FIGURES

LIST OF SYMBOLS AND ACRONYMS

VP	Vibratory Peening
SP	Shot Peening
VF	Vibratory Finishing
DEM	Discrete Element Method
FEM	Finite Element Method
CFD	Computational Fluid Dynamics
FFT	Fast Fourier Transforms
JKR	Johnson-Kendall-Robertson

CHAPTER 1 INTRODUCTION

Shot peening (SP) is a surface enhancement process that can increase fatigue life of metallic parts by as much as 20 times, when compared to the as-machined parts [1]. SP consists in blasting spherical particles at high velocity on a metal part, which generates in-plane plastic deformations that induce a layer of compressive residual stresses and cold working. The shot peening process increases fatigue life because the surface compressive residual stresses delay crack initiation. However, SP increases surface roughness that is unfavorable to fatigue life since it acts as local stress concentrations. A post finishing process is usually applied onto the shot peened part to reduce surface roughness [2].

The vibratory finishing (VF) process is a mass finishing process developed for polishing, deburring and cleaning small workpieces. This process consists in vibrating a tub filled with polishing media. The workpieces are inserted inside the polishing media and the vibrations induce a relative motion between the workpiece and the media particles, which polishes the workpieces [3].

The vibratory peening (VP) process is a manufacturing finishing process that combines both SP and VF by fixing the workpiece in the tub filled with media. The impact kinectic energy transmitted to the treated surface is higher, when compared to the vibratory finishing process, due to the fact that the fixed workpiece is submitted to higher velocity impacts. VP induces similar effects to those of SP on the workpiece, such as compressive residual stresses, while decreasing the surface roughness simultaneously. Therefore, it couples the same effects of both SP and VF.

The purpose of this study was to assess the motion of the media inside a vibratory peening machine. This study is essential to understand the behavior of both the vibratory peening machine and the impacts between the media and the treated part. It is a preliminary study that aims to guide further the modelling of the vibratory peening process.

This research was carried out in collaboration with Safran France, Centre Technologique en Aérospatiale (CTA) and VibraFinish Ltd. Safran France is an international group involved in aerospace and defense. They provided specimens made of Ti-6Al-4V and steel E16NCD13 that were studied in the research. CTA is a collegial technological transfer center that carries out applied research and development projects with the aerospace industry. VibraFinish Ltd is a Canadian SME specialized in vibratory finishing, shot blasting and other finishing processes. They provided the vibratory peening machine used for this study. The funding was provided by Safran France and by Natural Sciences and Engineering Research Council

of Canada (NSERC).

This thesis is divided in 6 chapters and organized as follows: Chapter 2 is a literature review on the vibratory peening process, the instrumentation of industrial vibratory machines and the modelling of vibratory finishing processes. Chapter 3 raises the scientific objectives related to this research. Chapter 4 presents the methodology of this work and Chapter 5 gives results of this work. Chapter 6 contains a general discussion of the obtained results and recommendations for future work.

CHAPTER 2 LITERATURE REVIEW

2.1 The vibratory peening process

2.1.1 Shot peening

Shot peening is a cold-working process that consists in projecting shot onto a ductile metallic part, at high velocity. The shot impacting the surface transmit energy that produces plastic deformation on the surface. The deformation stretches a surface layer with a thickness of few hundreds of microns. As the core of the material is not deformed, a residual stress field is induced in the material, leading to compressive residual stresses in the surface layer and tensile residual stresses in the core. The compressive stresses act as closure stresses that delay crack initiation and propagation [4]. The SP process also induces work hardening that increases the resistance to plastic deformation, specifically around the crack tip. However, the SP process induces roughness which has a detrimental effect on fatigue life [5]. The enhancement of fatigue life with shot peening is therefore a balance between its favorable and detrimental effects. The use of optimal conditions can improve fatigue lives up to 20 times [1], when compared to as-machined parts, or yields endurance fatigue limits 80% higher [6].

Shot peening relies on two process control parameters: Almen intensity and coverage. After SP, Almen strips bend progressively during the process progress due to plastic deformation. The Almen intensity induced by shot peening is defined as the arc height when doubling the peening time increases the arc height by 10 %. Figure 2.1 shows an Almen strip on an Almen holder (a) and an Almen gauge that measures the arc height. The strip is placed on four ball supports that encompass an area of 31.75 mm $\times$ 15.88 mm (b). Figure 2.1 (c) shows the saturation curve that is obtained by measuring the Almen strips' arc heights for different shot peening times. Coverage of a shot peened surface is defined by SAE J2277 [7] as the ratio (in percentage) of the surface indented by the shot to the total surface. Coverage is determined visually or by computer assisted image analysis.

Hong *et al.* [9] have modelled the shot peening process using the finite element method (FEM) to relate the shot peening parameters to the induced residual stresses. The authors used the finite element code ABAQUS Explicit to study the impact of single and multiple shot on a steel target with a density of 7800 kg/m^3, a Young's modulus of 200 GPa and an yield stress of 760 MPa. The target was a circular plate with a radius that was 8 times the diameter of the simulated shot. The shot was modelled as a rigid body. The diameter of the shot was 1 mm and the mass of the shot was 4.085 mg. A Coulomb law friction was applied between the

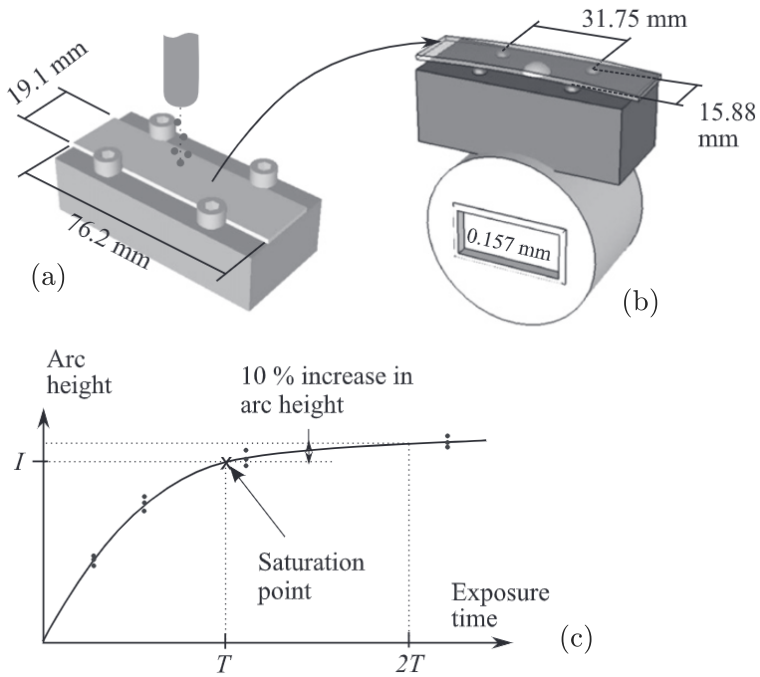

Figure 2.1 Description of the Almen intensity measurement procedure. (a) A SAE 1070 steel strip is held on an Almen holder while being shot peened. (b) After shot peening, the Almen strip is removed and set over a 31.75 mm × 15.88 mm area, and the arc height is measured using an Almen gauge. (c) The saturation curve is obtained by shot peening several Almen strips for numerous and repeated times of treatment. [8]

shot and the target with a coefficient $\mu = 0.2$. The impacting velocity was $v = 75$ m/s. The simulated results showed that the diameter of the shot had no influence on the magnitude of the surface residual stresses while the depth of compressive residual stresses zone increased linearly with the diameter of the media. Moreover, the impact velocity seems to have almost no effect on the magnitude of the surface residual stresses but velocity showed a significant effect on the maximum sub-surface residual stresses and the depth of the compressive residual stresses zone. Meguid *et al.* [10] found similar results for a steel target having the same density and Young's modulus as in Hong *et al.* [9]. The only difference in the parameters was the initial yield stress of 600 MPa in the study of Meguid *et al.* [10] and 760 MPa in the study of Hong *et al.* [9]. They found that shot velocity had no influence on maximum residual stresses whereas an increase of the shot diameter led to a deeper compressed layer.

2.1.2 Vibratory finishing

Vibratory finishing was introduced in the inudstry in the middle of the 20th century and widely used as a finishing process in the 60's. However, only a small amount of research was

done before the 70's. A vibratory finisher consists of a tub filled with media that oscillates on springs and in which parts are free to move. A motor is attached to the tub and drives two unbalanced shafts. Therefore, different modes of vibration can be created to fluidize the media by selecting the media mass, the media physical properties, the eccentricity of the shaft, the motor rotation frequency or the stiffness of the springs.

Yabuki *et al.* showed, by using a novel sensor placed in the part, that the drier the media is, the stronger is the abrasive effect [11]. Therefore, to avoid the abrasive effect, media is usually lubricated to clean itself and the treated part, to improve the media flow and to reduce the heat accumulation due to the friction between the parts and the media. Therefore, lubricating the media results in superior surface finish because the media flow is more fluid on the workpiece. Some lubricants contain acids to improve the finishing process [2]. The nature of the media is therefore key and must be carefully chosen as a function of the target surface finish [12]. There is therefore an extensive range of geometries, materials and media roughness that can be selected. Plastic, ceramic and steel media are mostly used.

Hashimoto *et al.* [3] examinated the consequence of several eccentric weights disposition in a bowl-type finisher on media flow using analytical and experimental studies. The authors found an optimal disposition of eccentric weights to widen the amplitude range of vibration of their vibratory finishing machine. One of the main issues in analyzing the experiments of the processes is the observation of the media inside the container. Thus, Naeini *et al.* [13] observed one layer of the media flow in a tub-type finisher using transparent walls on their machine to measure its bulk velocity. They compared the 2D velocities magnitudes of particles using discrete element simulations and compared with velocities magnitudes experimentally measured and obtained adequate media flow rate estimations. For 50 and 400 shots, the authors were able to estimate the shot velocities within 10% of the experimentally measured values. Hashemnia *et al.* [14] studied the media flow of a tub-type finisher using a visco-plastic finite element continuum model. The authors implemented the model using parameters computed from a discrete element model of the media bed. They validated their model by comparing the vertical position of several shot through the window of their vibratory finishing bowl with the vertical position of the tub experimentally measured using the laser sensors installed by Hashemnia *et al.* [15]. Hashemnia *et al.* [14] demonstrated that a continuum model produced similar impact shear rate and impact velocities of particles against the wall as a discrete model, with an average difference of 15% for one eighth of the computational time reported in Hashemnia *et al.* [15]. Mediratta *et al.* [16] developped a free impact model to understand what parameters have the most significant effects on plastic deformation during the vibratory finishing process. A free impact model is a contact model that considers one single point of contact between two impacting elements. The authors showed that frequency is the pa-

rameter that influences the most the Almen intensity during the vibratory finishing process. The authors observed that the process induced plastic deformation and material removal on the treated workpiece. One of the key parameters is also the choice of media, which means that size, density and hardness must be carefully chosen for the given problem. The model of Madiratta *et al.* [16] model could demonstrate that normal forces and high velocity have the largest impact on plastic deformation.

2.1.3 Vibratory peening

A vibratory peening machine is similar to a vibratory finishing machine. The main difference between the two processes is that the treated part is fixed to the machine's body during vibratory peening [17]. Therefore, for the vibratory peening process, the media impacts the treated surface with more energy due to the increase of relative velocity instead of sliding on the treated surface. Therefore, the impacts of media particles against the part cause the plastification of the treated surface, which induces compressive residual stresses from the surface down to approximately 130 μm.

A vibratory peening machine is composed of a tub filled with spherical and non-abrasive media, a suspension system, generally air bags because their stifness can be changed by controlling the pressure, and a motor that rotates shafts with eccentric masses to vibrate the tub. Figure 2.2(a) shows a schematic view of a vibratory peening machine in which the tub bounces on the base thanks to shafts mounted with eccentric masses and springs, as well as a view of the vibratory peening machine showing the motor that rotates the shafts. Figure 2.2(b) is the picture the eccentric weights and the springs while Figure 2.2(c) is the picture of the tub, the springs, the motor and the base.

The vibration frequency is controlled by the motor rotational speed and does not overstep 60 Hz. As in the vibratory finishing process, lubricant flows inside the tub, removes dust from the media and decreases heat accumulation.

A number of authors also related the process parameters to resulting roughness, residual stresses and fatigue life on AA7050-T7451 and AA3003-H14 [17,18], on titanium alloy Ti-6Al-4V [19] and on Inconel 718 [20]. Wang *et al.* [21] vibratory peened at 3.3 Hz a sintered 316LSC stainless steel speciment and showed that the process increased the corrosion performance by a factor of 1.4. Very few studies have been reported on the effects of parameters such as frequency on Almen intensity during vibratory peening process [17–20, 22].

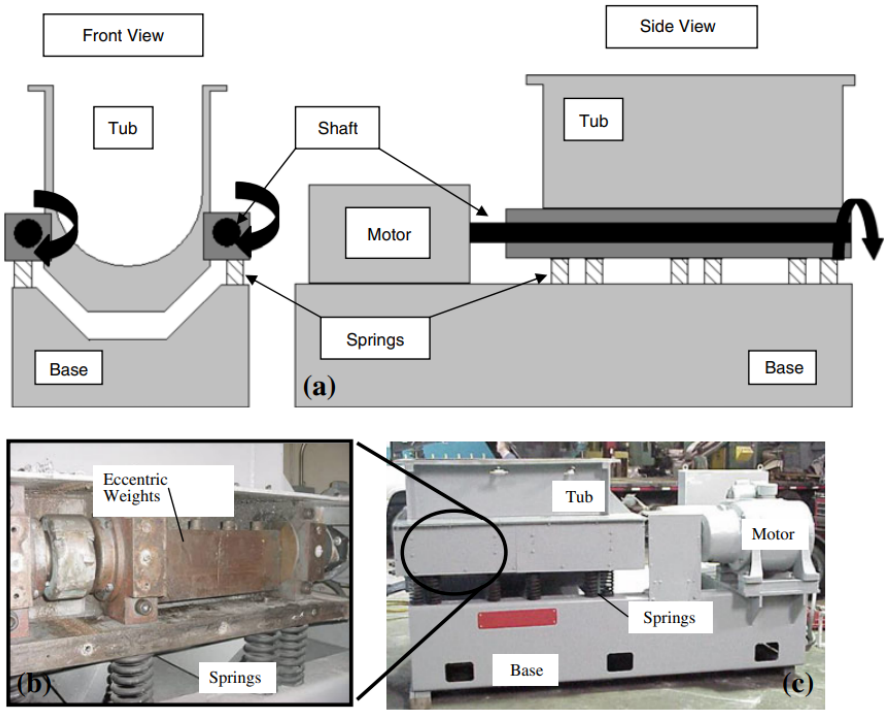

Figure 2.2 Schematic representation of a vibratory peening machine. (a) On the left side is the front view of the vibratory peening machine in which the tub bounces on the base thanks to the rotation of shafts mounted with eccentric masses and the presence of springs. The right side of the figure shows a side view of the vibratory peening machine with the motor that rotates the shafts. (b) Eccentric shafts and springs of the VP machine. (c) Tub that oscillates on springs due to the rotation of the shafts imposed by the motor [17].

2.1.4 Parameters that specify the vibratory peening process

Ciampini *et al.* [22] studied the effects of VP parameters on Almen intensity. They measured the impact velocity against the strip using a force sensor. They defined an adapted Almen system and found it appropriate to characterize the process efficiency because it combined all the process parameters into one measurement. Then, Ciampini *et al.* [23] developed a finite element model to predict the curvature of the vibratory peened Almen-like aluminium strips. They concluded that the Almen intensity was a function of the absorbed energy, diameter of the particle, material properties of the particle and strip thickness. Canals *et al.* [7] submitted Almen-like strips made of E-16NiCrMo13 steel and Ti-6Al-4V titanium alloy to VP and SP. The length, width and thickness for strips are 76 mm, 19 mm and 0.8 mm, respectively. The authors concluded that the range of Almen intensity obtained on the strips with both conventional shot peening and vibratory peening is from 0.12 mmA to 0.25 mmA.

The authors showed that for both materials, Almen intensity saturated after a certain time called T_{sat} of 12 minutes for a tub filled with 555 kg of media and shafts rotating at 47 Hz. Moreover, the authors noticed that VP has very little effect on hardness.

2.1.5 Comparison of VP, VF and SP in terms of surface characteristics, residual stresses and fatigue lives

Gane *et al.* [19] compared the fatigue life of Ti-6Al-4V flat notched specimens treated with VF and VP. The specimens were treated by VP for one hour in a tub filled with 4 mm and 7 mm spherical steel particles. The amplitude of vibration was 4 mm. The VF process was applied with 10 mm triangular ceramic media with an amplitude of 2.5 mm and the same processing time as VP. Both specimens were fixed in the container. Fatigue tests were perfomed at amplitude of 550 MPa, a stress ratio of -0.2 and a cycle frequency of 20 Hz. The fatigue life results demonstrated that VP yielded a fatigue life that was twice of that induced by the VF process.

Miao *et al.* [24] compared the effects of VP and SP in terms of surface roughness, residual stresses and fatigue life on AA7050-T7451 specimens. SP was performed with ceramic shot Z425 at an Almen intensity of 0.2 mmA and for 100% coverage. VP was performed with a mixture of hard steel particles (3 mm, 4.5 mm, and 6 mm in diameter). The media mass was 789 kg and the amplitude of vibration was 9 mm, at a frequency 50 Hz. The roughness measurements showed that the arithmetic mean surface roughness R_a increased by 656% after SP, when compared to that of the as-machined specimens. The largest peak to valley height R_t increased by 772%, when compared to that of the as-machined specimens. VP decreased R_a by 25% and R_t by 16%, when compared to those of the as-machined specimens. The authors also showed that, for a similar Almen intensity of 0.2 mmA, the SP process induced surface compressive residual stresses of 212 MPa while it was of 148 MPa by the VP process. However, the SP process induced maximum compressive residual stresses of 297 MPa while the VP process induced maximum compressive residual stresses of 225 MPa. However, VP induced the same residual stresses as SP at a depth of 520 μm below the surface. The authors also compared fatigue lives for specimens submitted to low cycle fatigue (LCF) testing with σ_{max} = 450 MPa and high cycle fatigue (HCF) where σ_{max} = 310 MPa and a ratio of 0.1. VP and SP led to the same LCF lives of 25 000 cycles and HCF lives of 250 000 cycles.

Feldmann *et al.* [20] compared the effects of the VP and SP processes on surface roughness of full blisk-rotors made of a nickel based alloy with two types of media: hard media and soft media. The materials of the media were not disclosed in their work. They found that VP led to an average surface roughness R_a of 0.15 μm with hard media and of 0.21 μm with soft

media, while SP produced R_a of 0.41 μm. SP induced surface compressive residual stresses were 13% more compressive than those obtained by VP. However, the maximum compressive stresses were similar for both processes and the residual stresses profile resulting from VP was 85% deeper, when compared to that resulting from SP. Specimens treated by shot peening with hard media led to fatigue strenght 16% higher than those treated by vibratory peening.

This limited survey showed that SP globally achieves higher compressive stresses, which is the most strengthening factor to improve the fatigue performance. However, Canals *et al.* [7] showed that for Almen-like strips made of E-16NiCrMo13 steel and Ti-6Al-4V titanium alloy, VP produces a similar range of Almen intensity as with SP. However, VP yielded much better surface finishes than SP that comes from the vibratory finishing effect. Therefore, it is possible that VP could deliver higher fatigue lives than SP by combining the vibratory finishing and shot peening in one single step.

2.2 Monitoring of the vibratory peening machine

2.2.1 Description of the vibratory motion

A vibratory machine is usually idealized as a combination of elements linked with springs and dampers. Those springs, dampers and mass of the parts of the vibratory peening machine help to define its modes of vibration of the machine. Air bags can be represented as springs and the rotating shafts are modelled with an eccentric mass that rotates oppositely to impose a vertical motion, as shown in Figure 2.3.

Hashimoto *et al.* [25] developed an analytical model of a bowl type vibratory finishing machine under free and forced vibrations with 5 degrees of freedom, the 3 translations and 2 rotations around the horizontal directions. The bowl was filled with spherical media having a diameter of 5 mm and were made of Al_2O_3. The treated work piece was modelled with 62 HRC steel. The authors used an acceleration sensor to measure the vibrations. Using this analytical model, the authors identified that the largest amplitude of vibration was 0.8 mm in the vertical direction. It was obtained when the eccentric mass on each shaft were set up oppositely.

2.2.2 Existing devices to measure vibrations

One of the most common way to measure the vibrations on industrial machines is by using a piezoelectric sensor. Ghemari *et al.* [26] explained the principle of the piezoelectric sensor. It uses a seismic mass that vibrates and converts the mechanical signal into an electrical

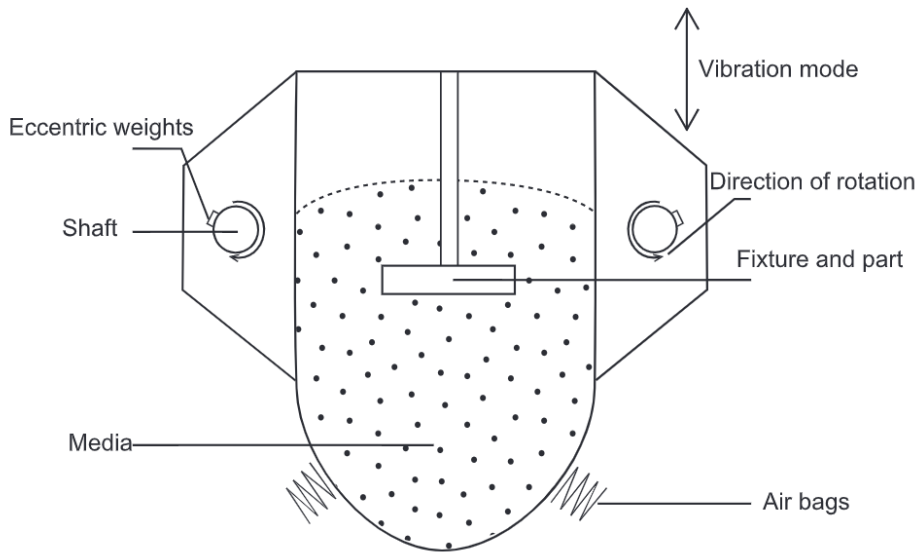

Figure 2.3 Model of a vibratory peening machines. Air bags are modelled using springs. The vibration mode is vertical because of the eccentric shaft rotation that induces vertical vibrations. The fixture and part are fixed inside the tub while media is free in the tub [7].

signal using piezoelectric elements. An analytical model of the displacement of the mass inside the sensor was developed to compare the experimental model of displacement of the mass in their research for an imposed amplitude and frequency of vibration. The system was modelled using a diagram made of a damper, a mass and a spring. Using this model and measurements of the sensor, the authors found out that the proposed sensor had an accuracy of 99.7%.

Liu *et al.* [27] used an experimental set up in which an oscillating motion was imposed on carbon plates, from 0 to 12.5 Hz, to measure vibrations modes. They used a kinect V2 sensor that allows to control an interface without a controller. The principle of this sensor works on optical properties and a neural network that helps recognize the observed object. The aim of this study was to predict the frequency of vibration of different vibrating objects. This method works only for measurements in one direction. It should be noted that this method is limited by the drawbacks of the Kinect depth sensor. Indeed, it cannot take into account all the displacement components of the target objects.

Wu *et al.* [28] also used an optical method to measure the vibrations of a bridge model. They used unmanned aerial vehicle (UAV) to track the bridge model by the digital image correlation (DIC) method. Their method assumes that vibrations are in the plane of the tracked images. Therefore, they cannot track the vibration component perpendicularly to

the images plane. However, their method can catch both plannar vibrations and deformation of the bridge.

Another way of measuring the vibrations of vibratory machines is to directly measure the rotation of the eccentric shaft used for imposing the vibrations. Reda *et al.* [29] placed a marker on the unbalanced shafts. Then, the electrostatic sensor detected the markers and evaluated their distance with the shaft. This method is usually used for static unbalance but the authors have shown that it can be used for frequencies under 15.9 Hz.

Hashemnia *et al.* [15] relied on laser sensors to track the displacement of a vibratory peening machine. Indeed, the authors used a laser sensor to measure the impact velocities of steel particles against a workpiece in a vibratory finisher. They showed that the measurement error for the impact velocity of a steel ball during a drop test was of 0.6 %.

The study of Hashimoto *et al.* [25] was the only one that detailed the 3D measurement of a vibratory finisher. They used piezoelectric sensor to measure the displacements and the rotations of the machine. However, no such detailed study has been found about the 3D monitoring of a vibratory peening machine.

2.3 Numerical modelling of a granular media flow

2.3.1 Description of a granular media flow

The geometrical parameters of the media and the associated forces and torque define a granular media flow. The geometrical parameters include the shape of the media particles, their initial positions and velocities. The forces and torque must be defined to solve the equations of dynamics as follows:

$$m\dot{\overrightarrow{U}} = \Sigma_n \overrightarrow{f}_n + \overrightarrow{F_{ext}}, \tag{2.1}$$

$$I\dot{\overrightarrow{\omega}} = \Sigma_n \delta_n \overrightarrow{c}^n \times \overrightarrow{f}_n + \overrightarrow{M_{ext}}, \tag{2.2}$$

where m and I are the mass and the inertia torque of one particle, respectively, $\overrightarrow{U}$ is the velocity vector of the particle, $\overrightarrow{f}_n$ is the contact force for each contact n, $\overrightarrow{c}^n$ is the unit contact vector that represents the direction of the overlap between the particle and an external particle, $\overrightarrow{F_{ext}}$ and $\overrightarrow{M_{ext}}$ represent the external forces and torque applied on the particle due to external forces. The contact condition is defined as $\delta_n < 0$ that corresponds to the overlap of one particle on another one [30]. Figure 2.4 illustrates $\delta_n < 0$ and f_n represents the strictly

positive contact force if the condition $\delta_n < 0$ is verified. If not, $f_n = 0$ N.

Radjai *et al.* [30] explains that only the velocity and the displacement are needed to compute the motion. The elasticity is not directly implemented in their model. The contact forces are computed thanks to δ_n and different laws of contact can be used according to the problem that has to be modelled [31].

Cotzee *et al.* [31] have shown that there is an equivalence between the contact parameters and the material properties such as Young's modulus and Poisson's coefficient. The authors developped and implemented in a Particle Flow Code (PFC) the Hertz-Mindlin model with Johnson-Kendall-Roberts (JKR) in which they expressed the normal and tangent contact forces determined with material properties of the model according to overlap δ_n as shown in Figure 2.5. The shear force is linear with displacement in shear direction in the author's model and the shear stiffness k_s^t is defined as:

$$k_s^t = 8G\sqrt{(\frac{1}{r_i} + \frac{1}{r_j})^{-1} * \delta_n}, \tag{2.3}$$

with G the effective shear modulus, r_i the radius of particle i, r_j the radius of particle j. The rolling resistance model is a Type C model that defines the resistance moment with k_s^t and μ the rolling friction coefficient. Therefore, Martin [32] explained that this model allows to implement in a DEM code physically-based contact law based on the material properties of the particles simulated. Those laws come usually from analytical derivations on a pair of spherical particles.

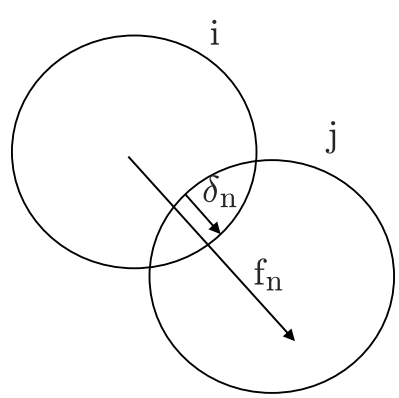

Figure 2.4 Illustration of detecting contact between 2 particles i and j using δ_n. The particles i and j are in contact when $\delta_n < 0$ and therefore a force of contact f_n is applied on both particles i and j.

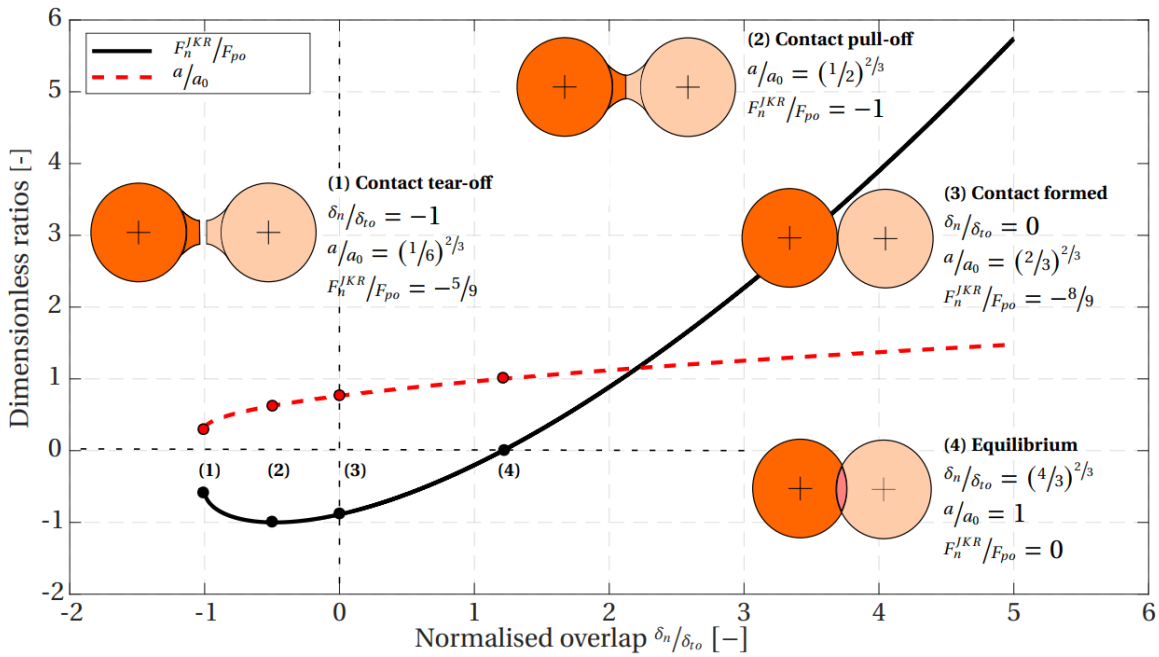

Figure 2.5 The contact model Hertz-Mindlin with JKR shows the relationship between the overlap δ_n and the associated force of contact f_n. The normalised force F_n^{JKR}/F_{po} and normalised patch radius a/a_0 against the normalised overlap δ_n/δ_{t0} is plotted. F_n^{JKR} is the total contact force, F_{po} is the pull-off force, a is the contact pitch radius, a_0 is the contact pitch radius where $F_n^{JKR} = 0$ and δ_{t0} is the tear-off distance [31].

2.3.2 Modelling of the granular flow for the vibratory peening process

2.3.2.1 Modelling shot impact with the discrete elements method

Naeini *et al.* [34] built a DEM model to compute the glass media motion in a two-dimensional tub in which the shape of the bottom of the tub is round. Alcaraz *et al.* [33] developped a three-dimensional model of a Rolls-Royce gas turbine 3-stage blisk treated with the vibratory peening process. The media material was a stainless steel 420-grade satellite/ball-cone-shaped media having a hardness of 50–52 HRC. Figure 2.6 shows the 3D visualization of the blisk inside the vibratory peening machine using the EDEM software. For particle-particle and particle-geometry contact, the authors used the Hertz-Mindlin model and a standard rolling friction model. The resistance moment M_r is defined in the standard rolling friction model described by Sakaguchi *et al.* [35] as:

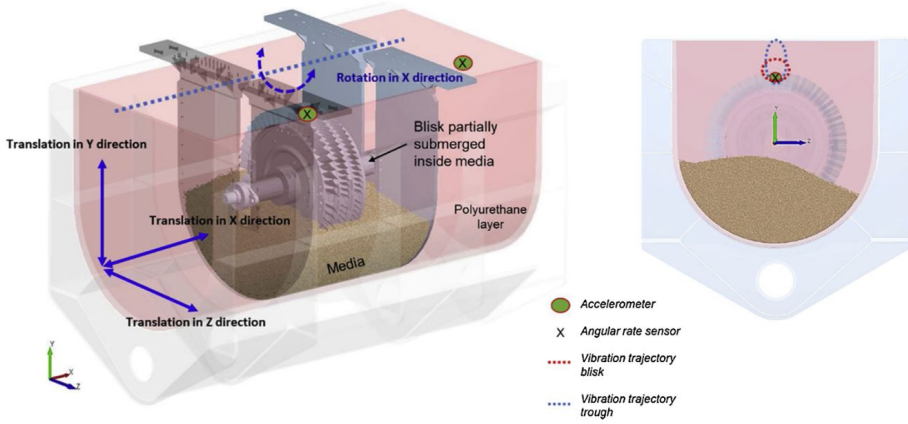

Figure 2.6 DEM model of vibratory peened blisk. On the left hand side is the 3D representation of the DEM model of the vibratory peening machine filled with media and the blisk as the workpiece. An accelerometer and an angular sensor have been set up on the VP machine. The right hand side shows a cut view perpendicular to the X direction [33].

$$M_r = -k_n a^2 \theta_r, \tag{2.4}$$

where k_n is the normal stiffness, a is the pitch radius and is defined as $a = (\frac{1}{r_i} + \frac{1}{r_j})^{-1}$ and θ_r is the relative rotation between two particles. Figure 2.6 shows an axial cut section of the DEM model. Figure 2.7 shows the relative velocity of the media. The authors found that the most significant effects in terms of compressive residual stresses on the coupons were observed when they were close to the free surface of the media. They also understood the motion of the particles and the areas of the blisk that were submitted to the highest impact velocities of the media. The normal force and relative velocity contributed to the peening effect of the compressive residual stresses whereas the tangential forces during contact contributed to the polishing effect by decreasing the roughness of the workpiece. The authors did not provide information about the time integrator scheme that was used and neither the time step. However, Blais *et al.* [36] explain that the explicit scheme Velocity Verlet can be used for DEM simulations for its stability, precision and low memory usage. To quantify the time step that must be used, the authors define the Rayleigh's wave propagation time as:

$$t_R = \frac{\pi r_{min}}{\chi} \sqrt{\frac{\rho_i}{G_i}}, \tag{2.5}$$

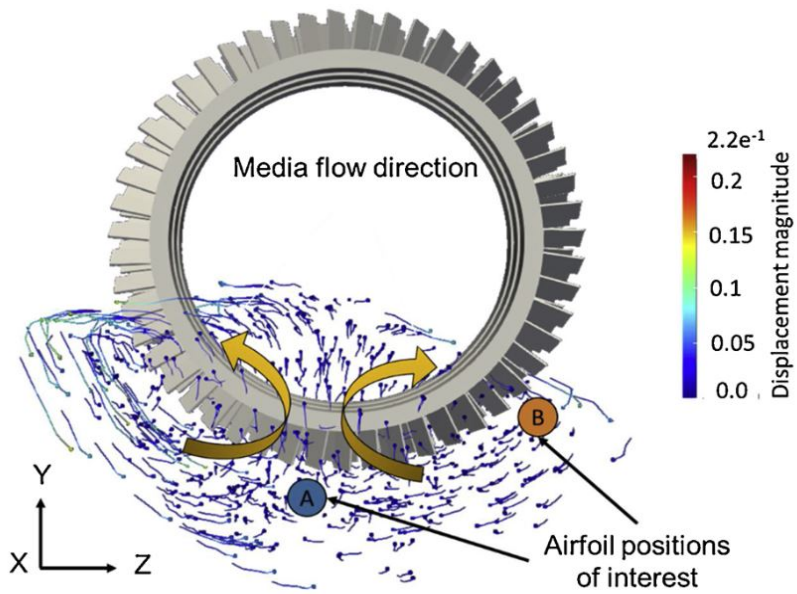

Figure 2.7 Media flow predicted with EDEM software for the case shown in Figure 2.6. Position A is the position where the impact velocity of media is the lowest on the coupons. Position B represents the position in the tub where the impact velocity of media against the coupons is the highest [33].

where r_{min} is the radius of the smallest simulated particle, $\chi = 0.8766 + 0.1631\nu_i$ with ν_i the Poisson coefficient of the particle, ρ_i is the density of the particle and G_i is the shear modulus of the particle. The authors explain that in practice, it is common to use a time step lower than 20% of the Rayleigh's wave propagation time.

To have the most relevant model with DEM, contact forces must be well defined. Giannis *et al.* [37] presented a solution for deformable particles. The classical deformable particles models consider the forces applied on a local space while all the particles have an impact on the applied forces. Therefore, the model presented is a multi contact strain based model that allows to account for the neighborhood of each particle. This method improved the accuracy of position prediction and velocity prediction of particles for very compact media, when compared to classical deformation methods.

The studies presented above suggest that the DEM technique can be successfully applied to simulate the VP process.

2.3.2.2 Finite elements method (FEM)

The finite element method is used when particles are fluidized or mixed [38]. Usually, this method is based on the Lagrangian frame in which the deformation of the media bed is computed [39]. The method is limited for granular flows because it induces large deformations and it is unable to represent the free surface of the media bed. Zheng *et al.* [38] used the FEM to model a granular flow in a rotating drum using an Eulerian frame. Therefore, a variable is needed to compute voids in the meshed Eulerian Volume Fraction (EVF). The granular media is considered as a continuous material using the Mohr-Coulomb elastoplastic (MCEP) model. The system as shown in Figure 2.8 is represented at a mesoscopic scale, which does not provide information on discrete features. However, it provides information about media bed internal stresses that the DEM cannot provide.

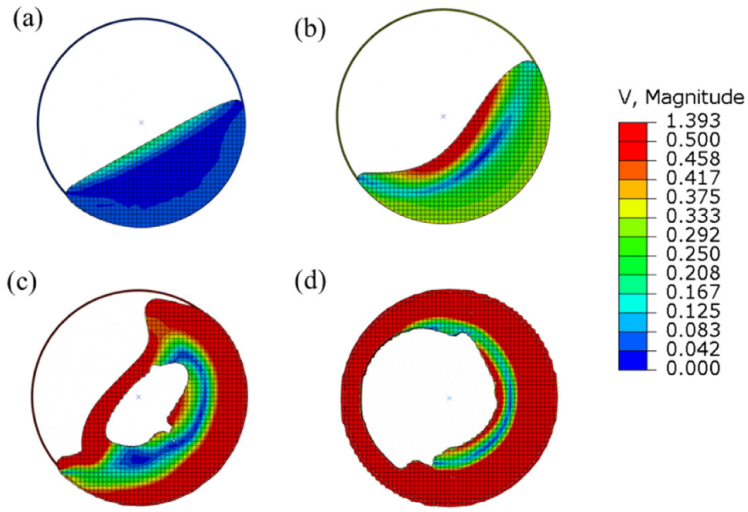

Figure 2.8 Motion of particles inside a rotating drum with the FEM, a) rotation at 10 rpm, b) rotation at 60 rpm, c) rotation at 150 rpm, d) rotation at 200 rpm. Particles are represented by a fixed mesh for which a velocity field is associated [38].

2.3.2.3 Computational fluids dynamics by the discrete elements method (CFD-DEM) and the discrete element method

Vijayan *et al.* [40] studied the efficiency of the mixing during the vibratory finishing process and detailed a solution to maximize the mixing of the media with a coupled CFD-DEM model. They used different size of particles and showed firstly that coupling the media with

a fluid flow increases the mixing of the particles. Then, without any fluid flow coupled to the media, the mixing of the media depends on its initial position. Indeed, when the densest particles are placed above the least dense, the mixing is more efficient. Their model also showed that a free surface increases the mixing, as presented in Figure 2.9. This study shows that the choice of several media particles has an effect on the particles position and therefore on the velocity inside the VF machine.

This survey suggests that the DEM is the most efficient method because it provides the information that is needed to understand the behavior of the media such as the normal forces and the impact velocities on the workpiece. Moreover, the media particles are commonly assumed as rigid bodies during the VP process, which promotes the use of the DEM method since it does not take into account the deformations of the target components during the simulations.

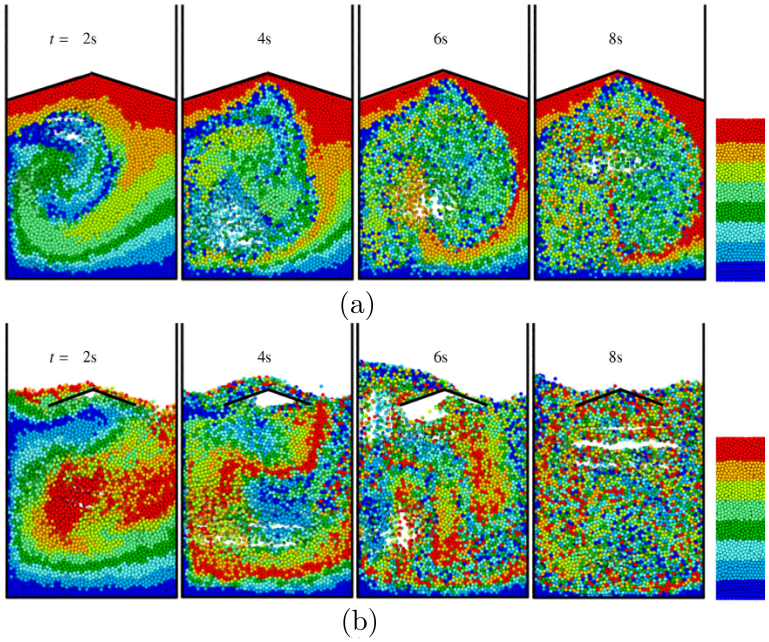

Figure 2.9 Motion of particles induced by a fluid flow. On the top simulation (a), the container is closed with a V plate whereas at the bottom simulation (b), the V plate is smaller so there is a free surface that allows a better mixing of the particles. The colors of the particles represent the initial layers at $t = 0$ s before the fluid flow is imposed from the bottom of the tub to the top of the static tub. The media is more free to move when the obstacle is small [40].

2.3.3 Analysis of literature and objectives

The literature review led to the following findings:

- Most of the research on Almen intensity was done by studying the vibration in one direction but not with a 3D frame. It is important to measure the motion in 3D to validate the assumption of a vertical motion of the vibratory peening machine.
- DEM is a relevant numerical method to model rigid bodies. The commercial software EDEM appeared to be a convenient software to simulate media flow in a vibratory peening machine.
- No studies have yet found a correlation between impact velocities of media and Almen intensity during vibratory peening.

To improve the knowledge in the literature about the simulation of the vibratory peening machine, a method of measurement of the tub motion is needed to understand the 3D behavior of the vibratory peening machine. Then, a relationship must be found between the kinematics of the vibratory peening machine and the impact velocity of media against a workpiece using a DEM model. The specific objectives were defined:

1- Monitor the vibratory peening machine using laser sensors.

2- Analyze the behavior of the vibratory peening tub and determine its modes of vibration.

3- Build a DEM model of the vibratory peening machine using the modes a vibration determined experimentally as input with the aim of obtaining the impact velocities of the media particles against an Almen strip that quantifies the intensity of the vibratory peening process.

CHAPTER 3 Monitoring of the vibratory peening machine

3.1 Experimental setup

The vibratory peening machine used for this project was manufactured by Vibra Finish Ltd and is shown in Figure 3.1. The operation consists firstly in fixing an Almen strip on a steel holder that is inserted into the media inside the tub and attached on the cover (see Figure 3.1(a) and (b)). The tub lies on airbags for which the inflation pressure can be changed (see Figure 3.1(d) and (e)). The vibrating motion is induced by eccentric masses on rotating shafts (see Figure 3.1(f)) controlled by the motor drive panel (see Figure 3.1(g)). A thermocouple was installed to measure the temperature near the Almen strip during operation (see Figure 3.1(c)).

Six banner laser sensors were installed to measure the amplitudes of the vibratory peening machine. The sensor range is [50 mm - 150 mm], the output signal is [4 mA – 20 mA] and the measurement/output frequency range is [250 Hz - 4000 Hz]. Figure 3.2 illustrates the locations of the six sensors on the three surfaces of the tub. Two sensors were installed on the top of the tub, one sensor in the front surface and three sensors on the right surface, as shown in Figure 3.2(a). The vibration amplitudes of the tub were computed with the measurements recorded from these six sensors. Figures 3.2(b), (c) and (d) show the location and installation of each sensor on the actual vibratory peening machine. Figure 3.3 details one sensor installation and indicates the correct functioning of one laser sensor.

A data acquisition system (DAS), supplied by National Instruments (cDAQ-9191), was used to collect the output signal of the six laser sensors. A LabVIEW interface, shown in Figure 3.4, was built to transform the output current from each laser sensor into the displacement value at each location, as shown in Figure 3.2. Figure 3.4 shows the LabVIEW interface that features three tabs. The first one named “Signals”, reports all the signals on the same figure. The second, “6 graphs”, shows all the signals on separated graphs. The third, “Configurations”, allows to set the sampling frequency that is 1000 Hz for all the measurements that have been made. Then, a Matlab program was developed to compute the movement of the whole tub for the simulation of the vibratory peening process.

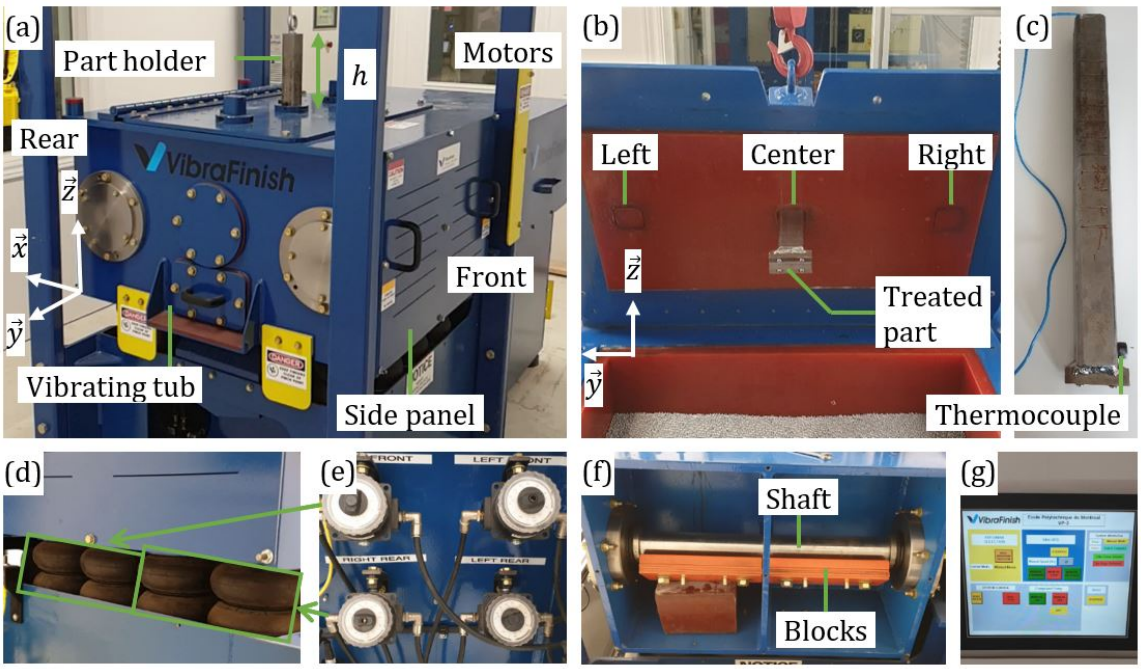

Figure 3.1 Images of the vibratory peening machine illustrating its operating parameters. (a) The vibrating tub is filled with media and the depth of the part inside the media is controlled by h, which is the height of the part holder above the tub. (b) The part holder is tightened at the center of the tub lid and two other positions (left and right) are available. (c) The part holder is equipped with a thermocouple to measure the temperature during the operation. (d) Two-pair airbags are located on each side of the tub. (e) The pressure in each pair is adjusted by a manometer. (f) The rotating shafts are behind the side panels. The number of blocks installed on the shafts determines the eccentricity. (g) The motor drive panel controls the motor speed.

3.2 Computation of the tub movement

Figure 3.5 shows the current locations of the six sensors (laser1 to laser6) and the definitions of the six studied surfaces (Plane A, Plane B, Plane C, Plane A', Plane B' and Plane C') as well as the eight studied corners (C_1 to C_8) for the computations of the tub movement. The external dimensions of the tub are defined as x_{tub}, y_{tub} and z_{tub} and are $1.1 \times 1.0 \times 0.9$ m^3. Each laser sensor records the displacement of each location on the tub where a laser points at. The coordinates of corner C6 of the tub is defined as (0, 0, 0), and the initial coordinates of the six sensors (x_i, y_i, z_i) are defined as the relative distance to the C6 corner of the tub when the machine is at rest (airbags pressure is $X_{Pres} = 0$ bar), and are ($x_1 = 0.05$ m, $y_1 = 0.05$ m, $z_1 = 0.9$ m), ($x_2 = 1.0$ m, $y_2 = 0.05$ m, $z_2 = 0.512$ m), ($x_3 = 0.851$ m, $y_3 = 0.915$ m, $z_3 = 0.90$ m), ($x_4 = 0.851$ m, $y_4 = 1.1$ m, $z_4 = 0.13$ m), ($x_5 = 0.09$ m, $y_5 = 1.1$ m, $z_5 = 0.13$ m), and ($x_6 = 0.09$ m, $y_6 = 1.1$ m, $z_6 = 0.512$ m), respectively. Those positions were measured

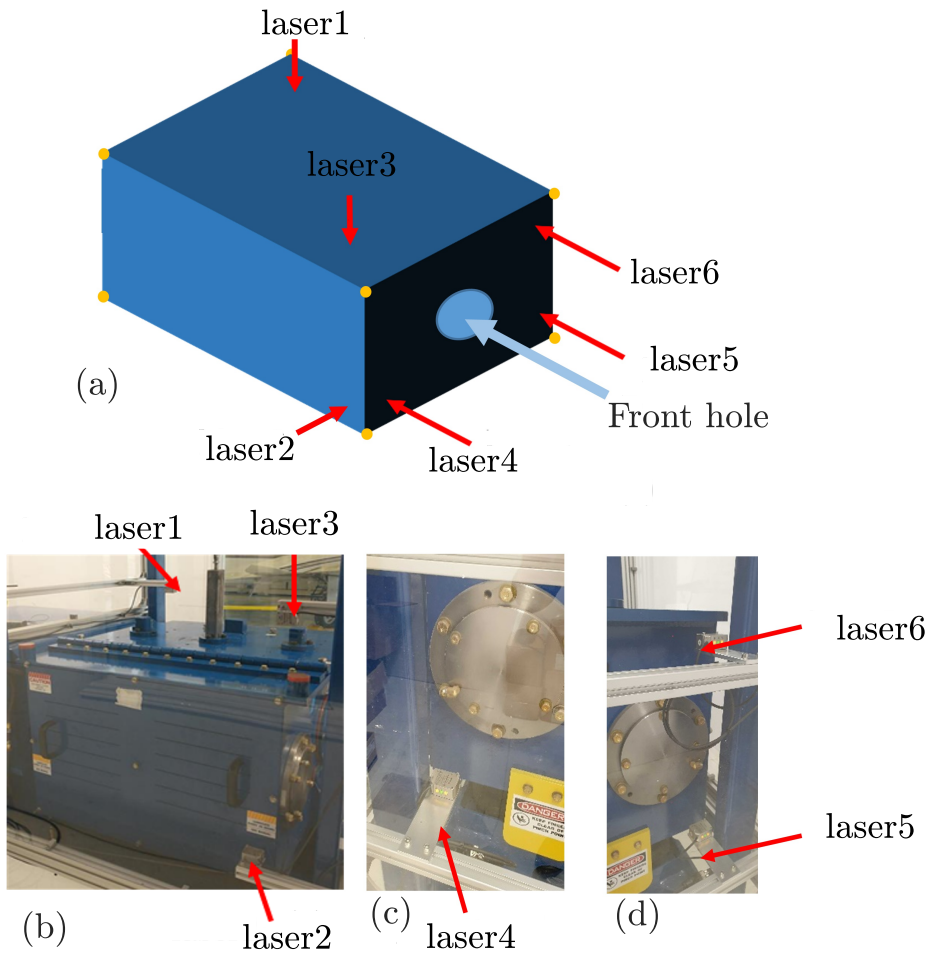

Figure 3.2 Installation of the six laser sensors at the three surfaces of the vibratory tub. (a) Location of the six laser sensors around the tub, (b) Installation of Sensor 1, Sensor 2 and Sensor 3, (c) Installation of Sensor 4, (d) Installation of Sensor 5 and Sensor 6.

with a measuring tape within ±1 mm. The recorded displacements of the six sensors were used to compute the orientations and orthonormal basis of the three planes, and then the displacements and the angles of rotation of the tub with respect to time, were computed according to the steps described in the following sub-sections.

Since the six lasers are all attached to the ground, they only measure the displacement parallel to the laser axis. For example, laser2 measures the tub's displacements in the x direction with zero value in y and z directions, lasers 4, 5 and 6 measure the tub's displacements in the y direction with zero values in x and z directions, lasers 1 and 3 measure the tub's displacements in the z direction with zero values in x and y directions. Therefore, $P_{laser_i}(t)$, the 3D displacement values of the ith laser, are defined as:

Figure 3.3 Installation of the sensor and the green light indicating the functioning of the laser Sensor 6.

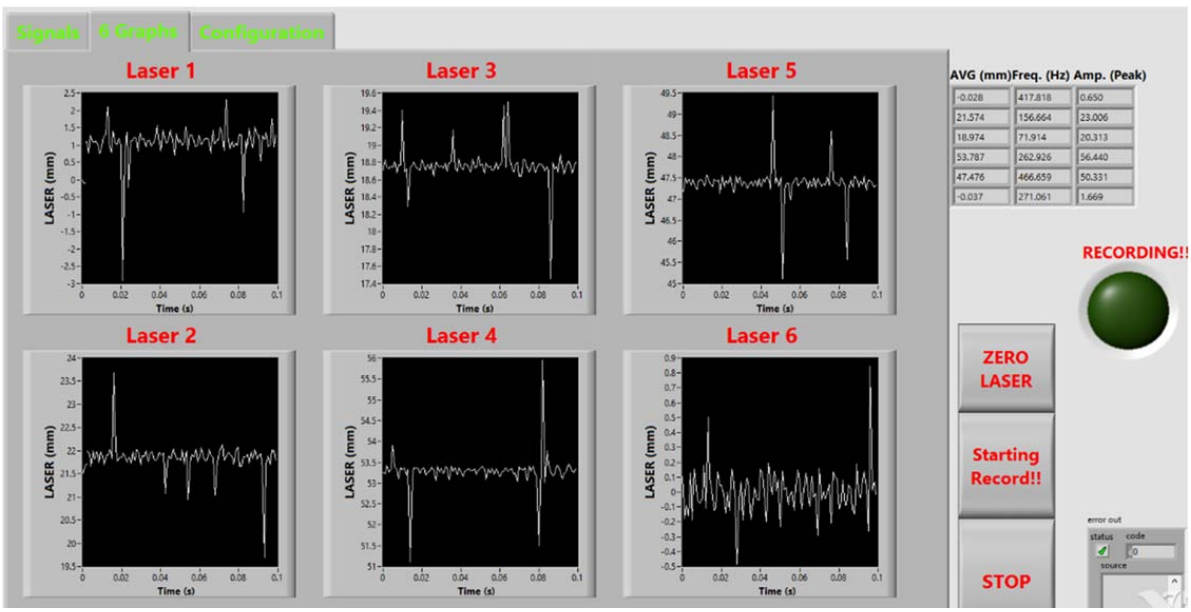

Figure 3.4 Displacement values from six sensors obtained by data acquisition system (DAS), from the LabVIEW interface for a snap shot of 0.1 second while the machine is operating at a steady state.

$$\{P_{\text{laser1}}(t)\} = \begin{bmatrix} x_1 \\ y_1 \\ z_1 - \text{laser}_{1\text{m}}(t) \end{bmatrix} = \begin{bmatrix} 0.05 \\ 0.05 \\ 0.9 - \text{laser}_{1\text{m}}(t) \end{bmatrix}, \tag{3.1}$$

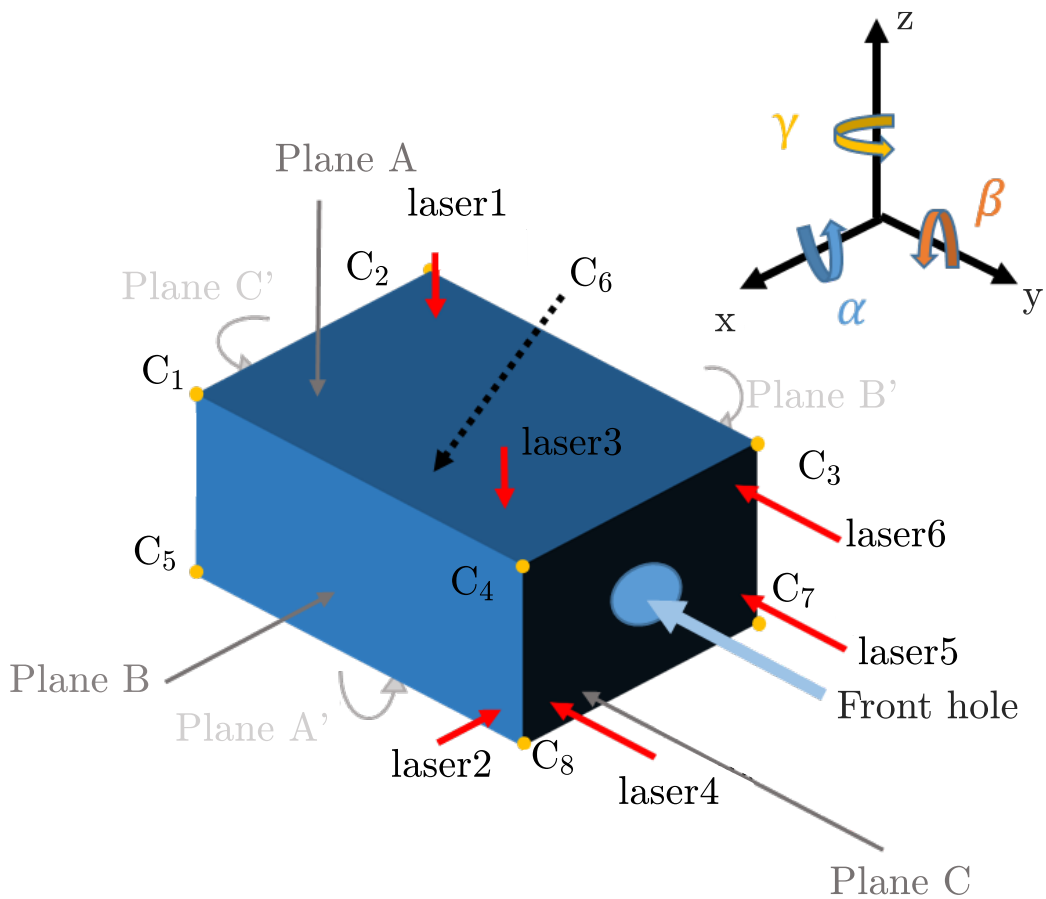

Figure 3.5 Location of the six sensors - Definition of directions (x, y, z), rotations (γ,β,α), external dimensions (x_{tub}, y_{tub} and z_{tub}), planes (A, A', B, B', C, C'), and eight corners (C_1 to C_8). (0, 0, 0) is located at the corner C_6.

$$\{P_{\text{laser2}}(t)\} = \begin{bmatrix} x_2 - \text{laser}_{2\text{m}}(t) \\ y_2 \\ z_2 \end{bmatrix} = \begin{bmatrix} 1.0 - \text{laser}_{2\text{m}}(t) \\ 0.05 \\ 0.512 \end{bmatrix}, \tag{3.2}$$

$$\{P_{\text{laser3}}(t)\} = \begin{bmatrix} x_3 \\ y_3 \\ z_3 - \text{laser}_{3\text{m}}(t) \end{bmatrix} = \begin{bmatrix} 0.851 \\ 0.915 \\ 0.9 - \text{laser}_{3\text{m}}(t) \end{bmatrix}, \tag{3.3}$$

$$\{P_{\text{laser4}}(t)\} = \begin{bmatrix} x_4 \\ y_4 - \text{laser}_{4\text{m}}(t) \\ z_4 \end{bmatrix} = \begin{bmatrix} 0.851 \\ 1.1 - \text{laser}_{4\text{m}}(t) \\ 0.13 \end{bmatrix}, \tag{3.4}$$

$$\{P_{\text{laser5}}(t)\} = \begin{bmatrix} x_5 \\ y_5 - \text{laser}_{\text{5m}}(t) \\ z_5 \end{bmatrix} = \begin{bmatrix} 0.09 \\ 1.1 - laser_{5m}(t) \\ 0.13 \end{bmatrix}, \tag{3.5}$$

$$\{P_{\text{laser6}}(t)\} = \begin{bmatrix} x_6 \\ y_6 - \text{laser}_{\text{6m}}(t) \\ z_6 \end{bmatrix} = \begin{bmatrix} 0.09 \\ 1.1 - \text{laser}_{\text{6m}}(t) \\ 0.512 \end{bmatrix}, \tag{3.6}$$

with $laser_{im}(t)$ being the recorded displacement values during the machine operation by sensor $i = [1, 6]$. The normal vectors of the three Planes A, B and C, which are $\{\overrightarrow{n_A}\}$, $\{\overrightarrow{n_B}\}$ and $\{\overrightarrow{n_C}\}$ can be computed as per.

$$\{\overrightarrow{v_{45}}\} = \{P_{laser5}(t)\} - \{P_{laser4}(t)\}, \tag{3.7}$$

$$\{\overrightarrow{v_{56}}\} = \{P_{laser6}(t)\} - \{P_{laser5}(t)\}, \tag{3.8}$$

$$\{\overrightarrow{n_C}\} = \frac{\{\overrightarrow{v_{45}}\} \times \{\overrightarrow{v_{56}}\}}{\|\{\overrightarrow{v_{45}}\} \times \{\overrightarrow{v_{56}}\}\|}, \tag{3.9}$$

$$\{\overrightarrow{v_{13}}\} = \{P_{laser3}(t)\} - \{P_{laser1}(t)\}, \tag{3.10}$$

$$\{\overrightarrow{n_A}\} = \frac{\{\overrightarrow{v_{13}}\} \times \{\overrightarrow{n_C}\}}{\|\{\overrightarrow{v_{13}}\} \times \{\overrightarrow{n_C}\}\|}, \tag{3.11}$$

$$\{\overrightarrow{n_B}\} = \{\overrightarrow{n_C}\} \times \{\overrightarrow{n_A}\}, \tag{3.12}$$

where $\{\overrightarrow{v_{45}}\}$ and $\{\overrightarrow{v_{56}}\}$ are the two vectors that are coplanar to Plane C, $\{\overrightarrow{v_{13}}\}$ is coplanar to Plane A.

Step 2: Compute the positions of the eight corners C_1 to C_8.

The position of a plane is defined as:

$$n_{\text{plane}_x} \cdot x + n_{\text{plane}_y} \cdot y + n_{\text{plane}_z} \cdot z = \delta, \tag{3.13}$$

where $(n_{\text{plane}_x},\ n_{\text{plane}_y},\ n_{\text{plane}_z})$ are the 3D coordinates of the normal vector of the plane,

δ is a constant, (x, y, z) are the coordinates of a point on the plane. For example, laser1 measurement lies on Plane A and the location of Plane A is compued as:

$$\delta_{\text{planeA}}(t) = n_{Ax} \cdot x_1 + n_{Ay} \cdot y_1 + n_{Az} \cdot (z_1 + laser_{1m}(t)). \tag{3.14}$$

Planes A', B' and C' are opposite and parallel respectively to Plane A, Plane B and Plane C, as shown in Figure 3.5. So the normal vectors are therefore:

$$n_{A'} = -n_A, \tag{3.15}$$

$$n_{B'} = -n_B, \tag{3.16}$$

$$n_{C'} = -n_C, \tag{3.17}$$

where $n_{A'}$,$n_{B'}$ and $n_{C'}$ are the normal vectors of Plane A', B', and C'. Notice that $n_{A'}$, $n_{B'}$ and $n_{C'}$ are defined as inward to the tub. This has been done to simplify the computation of matrix $M_{\gamma,\beta,\alpha}$ presented in (3.30). The constants of Plane A', B' and C' are computed by translating Plane A, B and C along their unit normal vector, which leads to:

$$\delta_{planeA'}(t) = \delta_{planeA}(t) - z_{tub}, \tag{3.18}$$

$$\delta_{planeB'}(t) = \delta_{planeB}(t) - x_{tub}, \tag{3.19}$$

$$\delta_{planeC'}(t) = \delta_{planeC}(t) - y_{tub}, \tag{3.20}$$

where $\delta_{planeA'}(t)$, $\delta_{planeB'}(t)$ and $\delta_{planeC'}(t)$ are the locations of Plane A', B' and C'.

Each corner is located at the intersection of three planes. Let's define $\{C\}^j$ and$\{D\}^j$, for $j = [1, 8]$ as:

$$\{C\}^1 = \begin{bmatrix} C_{1x} \\ C_{1y} \\ C_{1z} \end{bmatrix}, \{D\}^1 = \begin{bmatrix} \delta_{\text{plane}_B} \\ \delta_{\text{plane}_{C'}} \\ \delta_{\text{plane}_A} \end{bmatrix}, \tag{3.21}$$

$$\{C\}^2 = \begin{bmatrix} C_{2x} \\ C_{2y} \\ C_{2z} \end{bmatrix}, \{D\}^2 = \begin{bmatrix} \delta_{\text{plane}_{B'}} \\ \delta_{\text{plane}_{C'}} \\ \delta_{\text{plane}_A} \end{bmatrix}, \tag{3.22}$$

$$\{C\}^3 = \begin{bmatrix} C_{3x} \\ C_{3y} \\ C_{3z} \end{bmatrix}, \{D\}^3 = \begin{bmatrix} \delta_{\text{plane}_{B'}} \\ \delta_{\text{plane}_C} \\ \delta_{\text{plane}_A} \end{bmatrix}, \tag{3.23}$$

$$\{C\}^4 = \begin{bmatrix} C_{4x} \\ C_{4y} \\ C_{4z} \end{bmatrix}, \{D\}^4 = \begin{bmatrix} \delta_{\text{plane}_B} \\ \delta_{\text{plane}_C} \\ \delta_{\text{plane}_A} \end{bmatrix}, \tag{3.24}$$

$$\{C\}^5 = \begin{bmatrix} C_{5x} \\ C_{5y} \\ C_{5z} \end{bmatrix}, \{D\}^5 = \begin{bmatrix} \delta_{\text{plane}_B} \\ \delta_{\text{plane}_{C'}} \\ \delta_{planeA'} \end{bmatrix}, \tag{3.25}$$

$$\{C\}^6 = \begin{bmatrix} C_{6x} \\ C_{6y} \\ C_{6z} \end{bmatrix}, \{D\}^6 = \begin{bmatrix} \delta_{\text{plane}_{B'}} \\ \delta_{\text{plane}_{C'}} \\ \delta_{\text{plane}_{A'}} \end{bmatrix}, \tag{3.26}$$

$$\{C\}^7 = \begin{bmatrix} C_{7x} \\ C_{7y} \\ C_{7z} \end{bmatrix}, \{D\}^7 = \begin{bmatrix} \delta_{\text{plane}_{B'}} \\ \delta_{\text{plane}_C} \\ \delta_{\text{plane}_{A'}} \end{bmatrix}, \tag{3.27}$$

$$\{C\}^8 = \begin{bmatrix} C_{8x} \\ C_{8y} \\ C_{8z} \end{bmatrix}, \{D\}^8 = \begin{bmatrix} \delta_{\text{plane}_B} \\ \delta_{\text{plane}_C} \\ \delta_{\text{plane}_{A'}} \end{bmatrix}, \tag{3.28}$$

where $\{C\}^j$ is the location of corner j and the $\{D\}^j$ are the δ corresponding to the planes intersecting at corner j. By using Equation (3.13), the intersection of three planes can be computed by solving

$$\{D\}^j = [M] \cdot \{C\}^j, j = [1; 8], \tag{3.29}$$

for $\{C\}^j$. As per Equation (3.13), $[M]$ is defined as

$$[M] = \begin{bmatrix} n_{Bx} & n_{By} & n_{Bz} \\ n_{Cx} & n_{Cy} & n_{Cz} \\ n_{Ax} & n_{Ay} & n_{Az} \end{bmatrix}. \tag{3.30}$$

Since it is assumed that the tub is a prism with right angles, and since the vectors constituting $[M]$ are unit vectors, then $[M]$ is orthonormal, so that

$$\{C\}^j = [M]^T \cdot \{D\}^j, j = [1;8]. \tag{3.31}$$

Step 3: Compute the rotation and the displacement of the center of the tub.

The Euler angles (α, β, γ) are determined using the Matlab function `rotm2eul.m` that solves for γ, β and α

$$[M] = [\mathrm{rot}z(\gamma)] \cdot [\mathrm{rot}y(\beta)] \cdot [\mathrm{rot}x(\alpha)], \tag{3.32}$$

where

$$\mathrm{rot}z(\gamma) = \begin{bmatrix} \cos(\gamma) & -\sin(\gamma) & 0 \\ \sin(\gamma) & \cos(\gamma) & 0 \\ 0 & 0 & 1 \end{bmatrix}, \tag{3.33}$$

$$\mathrm{rot}y(\beta) = \begin{bmatrix} \cos(\beta) & 0 & \sin(\beta) \\ 0 & 1 & 0 \\ -\sin(\beta) & 0 & \cos(\beta) \end{bmatrix}, \tag{3.34}$$

and

$$\mathrm{rot}x(\alpha) = \begin{bmatrix} 1 & 0 & 0 \\ 0 & \cos(\alpha) & -\sin(\alpha) \\ 0 & \sin(\alpha) & \cos(\alpha) \end{bmatrix}. \tag{3.35}$$

Finally, the displacement of the center of tub is defined as the average displacement of the eight corners:

$$\{C\}^{Center} = \begin{bmatrix} U_x \\ U_y \\ U_z \end{bmatrix} = \sum_{i=1}^{8} \frac{\{C\}^j}{8}, \tag{3.36}$$

where $\{C\}^{Center}$ is a vector composed of the coordinates of the center of the tub, and U_x, U_y and U_z are the displacements of the center of tub along x, y and z directions, respectively.

3.3 Example of the computation of the tub movement

Using Equations (3.7) to (3.36), the rotations (α, β, γ) and displacements motion (U_x, U_y, U_z) of the center of the vibratory tub were computed. Figure 3.6 shows the measured

displacement values from the six lasers recorded during the operation of the vibratory peening machine for 1 second after it reached a stable movement and for the following operating conditions: shaft frequency $X_{Freq} = 25$ Hz, a media mass $X_{Mass} = 544$ kg, an eccentricity $X_{Ecc} = 24$ kg/shaft, airbags pressure $X_{Press} = 2.8$ bar, a media height above the part $X_{Height} = 150$ mm, a part's position X_{Pos} in the middle, and a lubricant rate $X_{Lub} = 20$ rpm. It can be seen that the displacements recorded by lasers 1 and 3 are much higher than any displacements from the other four lasers, which shows that the up and down movement is the dominant movement for the vibratory peening machine, similarly to what is observed in Figure 3.6.

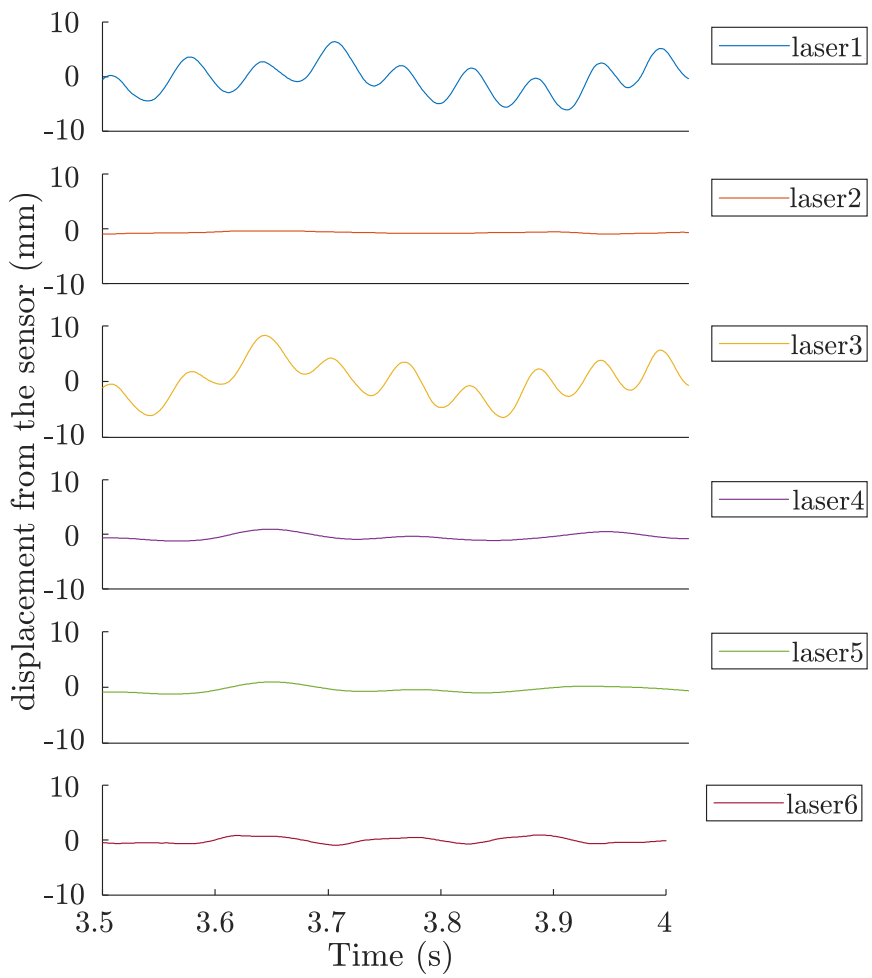

Figure 3.6 Measurements of the 6 sensors with vibratory peening conditions of $X_{Freq} = 25$ Hz, $X_{Mass} = 544$ kg, $X_{Ecc} = 24$ kg/shaft, $X_{Press} = 2.8$ bar, $X_{Height} = 150$ mm,X_{Pos} in the middle and $X_{Lub} = 20$ rpm. Vertical motion is captured by laser1 and laser3 and is dominant when compared to the horizontal displacements.

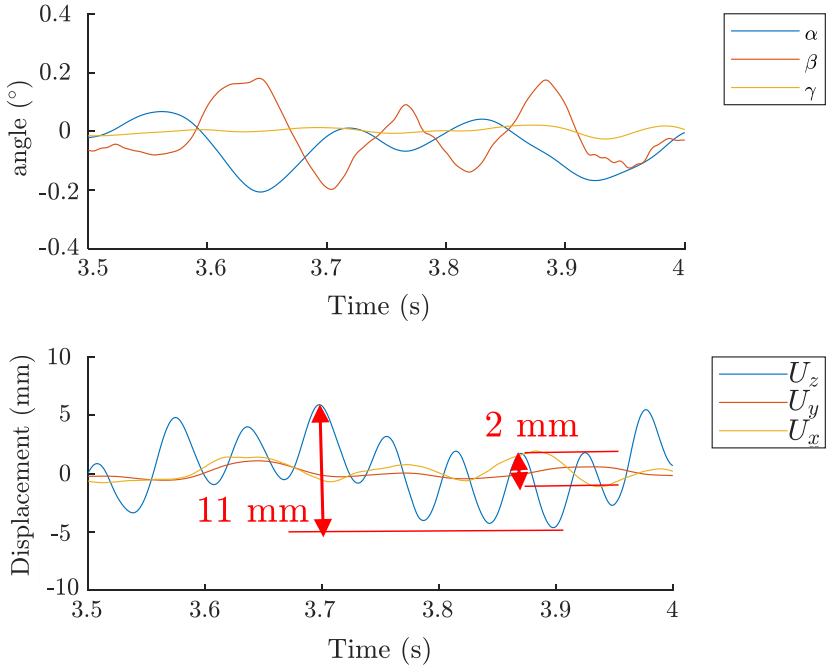

Figure 3.7 Computed rotations (a) and displacement $\begin{bmatrix} U1_x \\ U1_y \\ U1_z \end{bmatrix}$ (b) of the center of the tub with vibratory peening conditions of $X_{Freq} = 25$ Hz, $X_{Mass} = 544$ kg, $X_{Ecc} = 24$ kg/shaft, $X_{Press} = 2.8$ bar, $X_{Height} = 150$ mm, X_{Pos} in the middle and $X_{Lub} = 20$ rpm. The dominant motion is the vertical motion whereas angles of rotation are lower than 0.2° and will be neglected in the further simulations.

Figure 3.7 presents the computed rotation and displacement of the center of the tub as a function of time for of $X_{\text{Freq}} = 25$ Hz, $X_{\text{Mass}} = 544$ kg, $X_{Ecc} = 24$ kg/shaft, $X_{\text{Press}} = 2.8$ bar, $X_{\text{Height}} = 150$ mm, X_{Pos} in the middle and $X_{\text{Lub}} = 20$ rpm. The figure shows that the maximum amplitude of U_z is 11 mm, which is larger when compared to the maximum amplitudes U_x and U_y, which are of 2 mm and 1 mm respectively. The three rotation angles (α, β, γ) lie in the range of $[-0.3°, 0.2°]$, which suggests that the tub remains relatively at the same orientation during operation. Therefore, only U_z is considered as the vertical amplitude of the movement of the tub for further simulations of the vibratory peening process.

3.4 Induced displacement due to a 1 mm error of measurements of the lasers positions

An analysis has been done to demonstrate that a 1 mm error on the measurement of the position of the lasers does not significantly impact the computed tub position. The coordinates of the sensors with the induced error are ($x'_1 = 0.051$ m, $y'_1 = 0.05$ m, $z'_1 = 0.899$ m), ($x'_2 = 1.0$ m, $y'_2 = 0.05$ m, $z'_2 = 0.513$ m), ($x'_3 = 0.851$ m, $y'_3 = 0.914$ m, $z'_3 = 0.90$ m), ($x'_4 = 0.852$ m, $y'_4 = 1.1$ m, $z'_4 = 0.129$ m), ($x'_5 = 0.091$ m, $y'_5 = 1.1$ m, $z'_5 = 0.1295$ m), and ($x'_6 = 0.09$ m, $y'_6 = 1.1$ m, $z'_6 = 0.512$ m). The displacement of the center of the tub has been computed with the lasers measurements that have been presented in Figure 3.6 for this new setup of lasers.

The difference $\begin{bmatrix} e_x \\ e_y \\ e_z \end{bmatrix} = \begin{bmatrix} U'_x \\ U'_y \\ U'_z \end{bmatrix} - \begin{bmatrix} U1_x \\ U1_y \\ U1_z \end{bmatrix}$ is computed and plotted in Figure 3.8, where $\begin{bmatrix} U1_x \\ U1_y \\ U1_z \end{bmatrix}$ is the vector of displacements of the center of the tub without error of the measurements on the lasers position and $\begin{bmatrix} U'_x \\ U'_y \\ U'_z \end{bmatrix}$ the vector of displacements of the center of the tub with an error of 1 mm on the measurements on the lasers position. Figure 3.8 shows that a random error between -1 mm and +1 mm on each position of the sensor induces a maximum error of 5 μm.

A random error between -1 mm and 1 mm has been generated 1000 times on each sensor position to have a global idea of how big the maximum error is. So the same computations have been performed for 1000 random positions and for each of the 1000 iterations, the maximum error in absolute value is computed. Figure 3.9 shows that the maximum error in

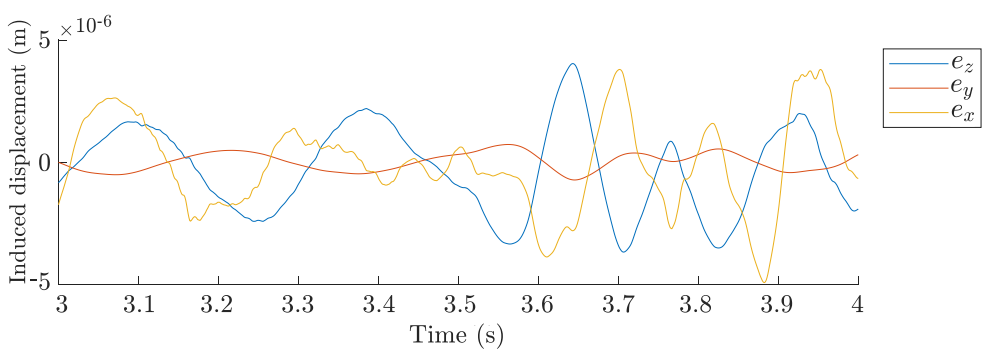

Figure 3.8 Induced displacement in the tub movement computation due to a 1 mm error of measurement of the position of the laser sensors.

the position of the center of the tub for the 3 directions is 16μm, which is acceptable for this study.

Note that the error has been induced in lasers positions but not in their orientations. A further analysis of the effect of a disorientation of the lasers could be done to validate further the robustness of the setup.

3.5 Validation of the measured tub rotation angle computation

The vibratory peening machine was intentionally tilted as shown in Figure 3.10 to validate the computation of the rotation angles. The positions (x, z), in pixels, of the two end points P_1 and P_2 in the tub were defined and measured using Loggerpro software that is a manual

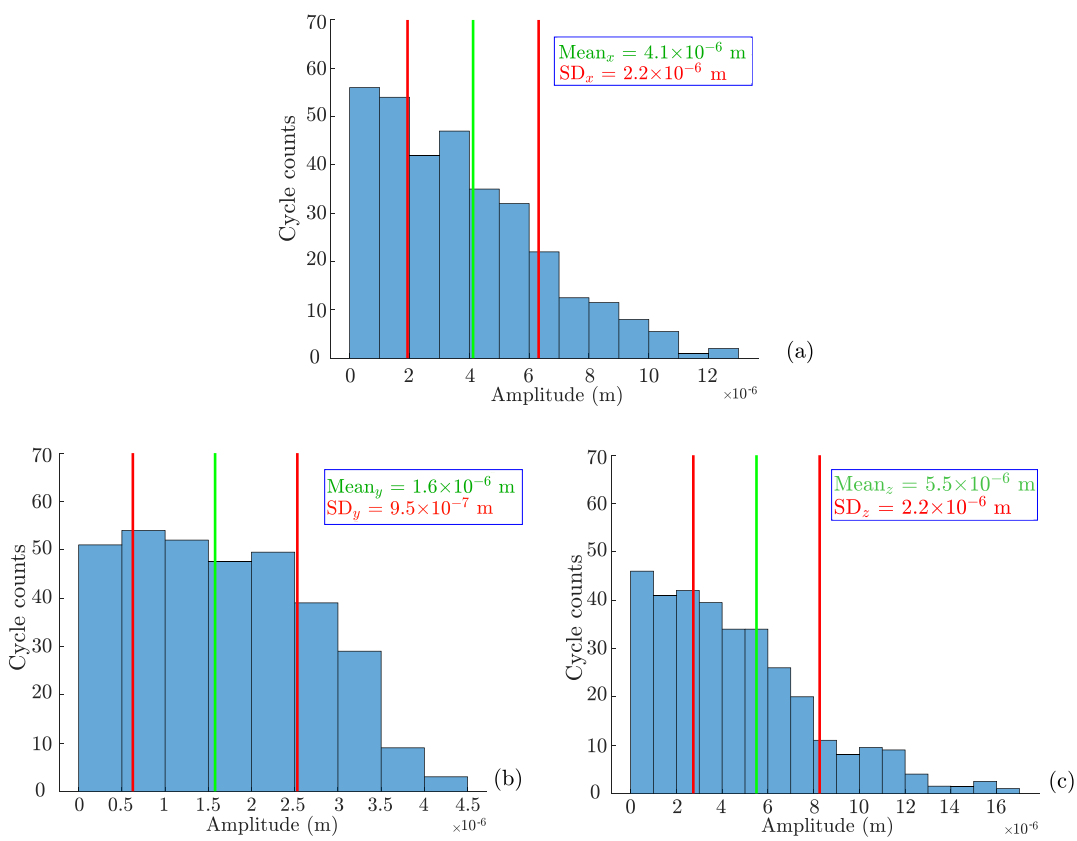

Figure 3.9 Histogram of induced displacement in the tub movement computation due to a 1 mm error of measurement of the position on the laser sensors in the 3 directions x a), y b) and z c) for 1000 random positions with a maximum error of measurement of 1 mm. The maximum error is 16μm. Red lines represent the standard deviation and the green line corresponds to the mean value of the amplitude variation due to the 1 mm error.

video tracking software as:

$$P_1 = \begin{pmatrix} x_1 \\ z_1 \end{pmatrix} = \begin{pmatrix} 606 \\ -210 \end{pmatrix}, \tag{3.37}$$

and

$$P_2 = \begin{pmatrix} x_2 \\ z_2 \end{pmatrix} = \begin{pmatrix} 606 \\ -210 \end{pmatrix}. \tag{3.38}$$

Therefore β_m, the measured maximum angle β illustrated in Figure 3.5, is computed as:

$$\beta_m = \arctan \frac{z_2 - z_1}{x_2 - x_1} = 3.22°. \tag{3.39}$$

The six lasers recorded the positions of the tub and the rotation angle β_{sim}, from Equation (3.32) using the `rotm2eul.m` Matlab function as 3.19°. The 0.9% difference between the β_{sim} and β_m could be due to the resolution of the picture. This level of similitude between the computed and experimentally measured angle is sufficient for our application.

3.6 Comparisons of the computed amplitudes with the recorded values from the laser sensors

Fourier transforms of the signals from the recorded displacements of lasers 1 and 3 in Figure 3.6 and the computed vertical displacement U_z in the center of tub in Figure 3.7 were computed by Matlab function `fft.m` and are presented in Figure 3.11 for comparison. The Fourier transforms extracts the discrete frequencies and the associated amplitudes of a periodic signal. The figure shows that, for a test at frequency of 25 Hz, the vertical amplitude

Figure 3.10 Computation of the angle of the tub using software logger pro to get the tilt illustrated by P_1 and P_2.

of the center of the tub (A = 1.8 mm) is similar to the amplitude of laser1 (A = 1.74 mm) with a relative difference of 2.2% and of laser3 (A = 1.87 mm) with a relative difference of 5%. Moreover, in Figures 3.11(b) and (c), two extra modes of vibration at 7 Hz and 13 Hz appear and disappear in Figure 3.11(a). This is due to the fact that laser1 and laser3 measure the displacement at 2 extremities of the tub. These modes are of opposite phase, which explains that they do not appear at the center of the tub. Therefore these modes represent the small rotations of the tub and must not be taken into account for another vertical mode of vibration.

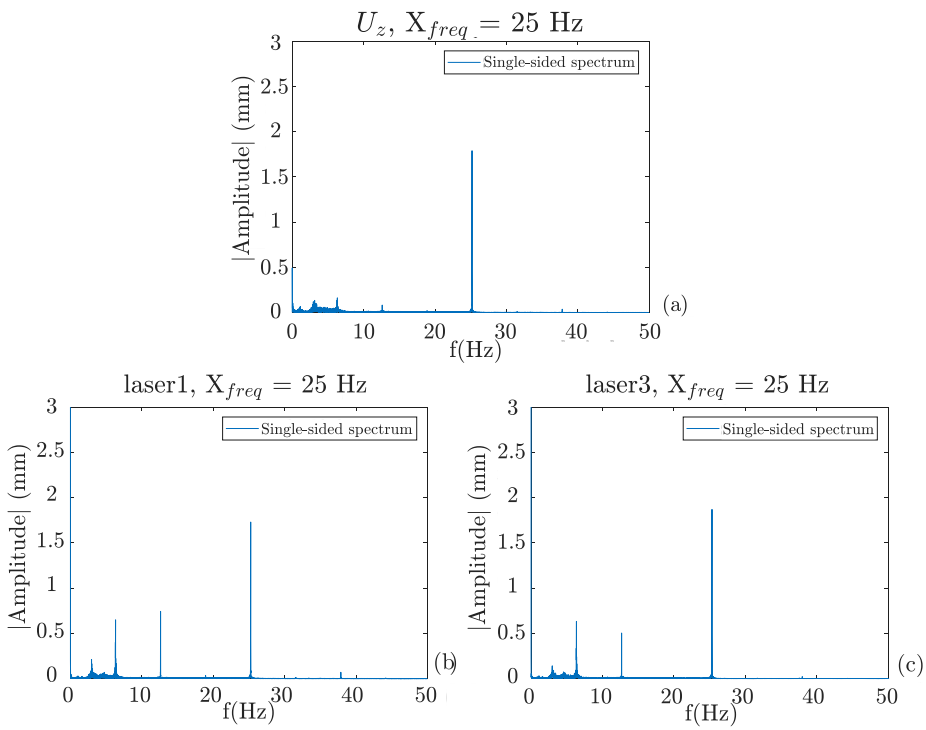

Figure 3.11 Comparison of the Fourier transform of the recorded displacements of laser1 and laser3 from Figure 3.6 and the computed U_z in Figure 3.7. (a) Fourier transform of U_z, (b) Fourier transform of laser1, (c) Fourier transform of laser3. The highest frequency corresponds to the same amplitude on each spectrum. Two low modes of vibration from laser1 and laser3 disappear in U_z because they correspond to the vibrations around x and y directions. It shows that 3D computation of the movement was necessary to understand that lowest modes of vibration correspond to the rotation of the tub whereas the highest mode of vibration corresponds to the actual vertical vibrations.

3.7 Conclusion

Six robust laser sensors have been installed to compute the motion of the machine. There is a little difference between the raw measurements of the vertical sensors and computed vertical displacement of the machine U_z. Moreover, the study shows that the lateral components of displacements, as well as the rotation angles, are comparatively small, which validates the hypothesis of a vertical displacement for the machine.

CHAPTER 4 Numerical modelling of the media flow inside the tub of the vibratory peening machine

4.1 Simulations of the movement of the media inside the tub

A DEM model was developed using the Software EDEM to simulate the media movement inside the vibratory peening tub to obtain the impact velocities of particles against the Almen strip, and to study the correlation between Almen intensity and the corresponding impact velocity against the strip. The simulations were based on the vibratory peening tests with shaft frequencies of 17.5, 20, 22.5, 25, 27.5 and 30 Hz, a media mass $X_{Mass} = 544$ kg, $X_{Ecc} =$ 24 kg/shaft, $X_{Press} = 2.8$ bar, $X_{Height} = 150$ mm, X_{Pos} in the middle and $X_{Lub} = 20$ rpm.

4.1.1 DEM model of vibratory peening

The dimensions of the actual vibratory peening tub are $500 \times 740 \times 500$ mm^3, the media mass is 544 kg, and the media diameter is 3 mm, which corresponds to approximately 4.1 millions media particles. Simulating the actual dimensions of the tub would take several days to represent 1 second of operation. To decrease the computational time, the dimensions have been reduced to $20 \times 500 \times 500$ mm^3 and $\frac{20\times500\times500}{500\times740\times500} \times 4.1 \times 10^6 = 1.1 \times 10^5$ steel particles were simulated. This number of particles allows to run a 1 second operating simulation in 1 hour, which was deemed acceptable. A Young's modulus $E_{steel} = 210$ GPa, a Poisson's ratio $\nu_{steel} = 0.3$, and a density $\rho_{steel} = 7800$ kg/m^3 were used to define the steel media. The vibratory peening tub is lined with rubber to prevent tub damage. Therefore, a rubber material having a Young's modulus $E_{rubber} = 0.001$ GPa and Poisson's ratio $\nu_{rubber} = 0.5$ was applied as material properties in the simulations for the tub liner. The treated material was cemented steel E16NCD13 and the specimens had dimensions of $19 \times 76 \times 0.81$ mm^3 for the N strip and $19 \times 76 \times 1.27$ mm^3 for the A strip. In the DEM model, a steel strip with dimensions of $20 \times 80 \times 1$ mm^3, a Young's modulus $E_{steel} = 210$ mm^3 and a Poisson's ratio $\nu_{steel} = 0.3$ were applied to simulate a treated part as similar as possible to the actual specimens. Notice that thickness does not impact the results of the computed impact velocity because no deformation was computed is the DEM model.

Figure 4.1 shows the sectional view of plane (y, z) of the DEM model with an Almen holder in the middle of the tub with same steel properties as those of the media. The dimensions of the holder are of $20 \times 100 \times 20$ mm^3 and the Almen strip dimensions are of $20 \times 76 \times 1$ mm^3. The depth between the bottom of the tub and the Almen strip is 250 mm. The thickness

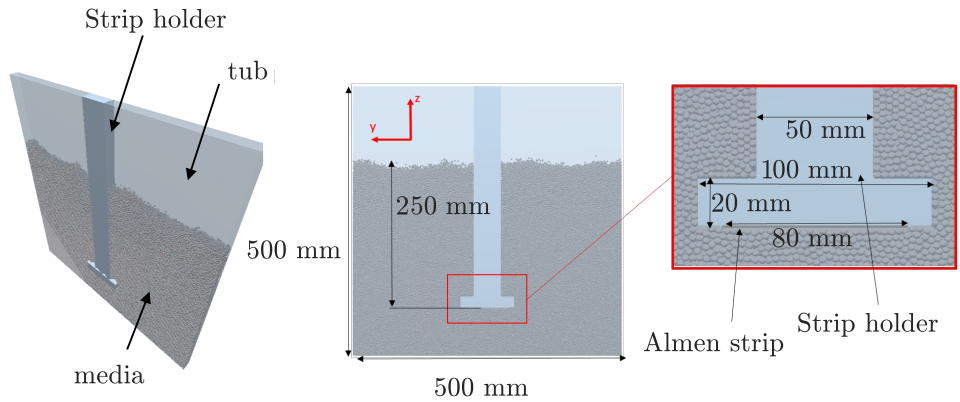

Figure 4.1 Visualization of the DEM model with 1.1×10^5 steel particles having diameter of 3 mm inside a tub having dimensions of $20 \times 500 \times 500$ mm^3. (a) 3D Visualization of the model (b) Sectional view of the DEM model (c) Zoom on the Almen specimen. The dimensions of the base of the holder are $20 \times 100 \times 20$ mm^3, which is identical to actual holder, and the Almen strip dimensions are $20 \times 80 \times 1$ mm^3. The distance between the bottom of the tub and Almen strip is 250 mm.

of the DEM model in the x direction in Figure 4.1 is 20 mm. The coefficient of restitution between two spherical steel impacting media is defined as 0.95 according to Lecornu [41]. The coefficient of restitution between the media and the Almen holder and between the media and the Almen strip was assumed to be of 0.95. The coefficient of restitution between particles and the tub was estimated manually by dropping one media onto the same rubber surface as the liner of the tub. The position of the initial drop and the position after one rebound was measured and used to compute the coefficient of restitution. The coefficient of restitution between the media and the rubber material is defined as:

$$CoR = \sqrt{\frac{H_{re}}{H_{ini}}}, \tag{4.1}$$

where H_{ini} is the height measured at the initial position and H_{re} is the measured height after the first rebound, as illustrated Figure 4.2. The drop tests were recorded with an iPhone X camera recording at 240 fps with a resolution of 1080 p. The height measurements were done with Loggerpro software that provides a manual tracking of the positions of the particle. The drop tests were carried out 10 times and the average of coefficient of restitution $CoR = 0.71$ was obtained. The maximum value was $CoR_{max} = 0.72$ and the minimum value obtained was $CoR_{min} = 0.70$. The coefficient of restitution between particles and rubber was set to 0.71.

The contact model used for the computations was the Hertz-Mindlin model with JKR in

which tangential and normal forces depend on the normal overlap δ_n described in Section 2.3.1. Since the media is lubricated during the operation, the model was assumed to have zero rolling friction and zero sliding friction. Since there is only one liter of lubricant for 544 kg of media mass during the operation, it is assumed that lubrication has no effect on the coefficient of restitution on the particle-particle interactions and particle-tub interactions. The applied time integrator was the Velocity Verlet scheme and the associated Rayleigh wave propagation time was $t_R = 1.58$ μs. The timestep Δt used for the time integration was 10 times lower than t_R, which was 1.58×10^{-7} s.

4.1.2 Conditions for the DEM simulations

The vibrating amplitude and frequency are the two inputs for the DEM simulation of the vibratory peening process. Six vibratory peening tests with shaft frequencies X_{Freq} of 17.5, 20, 22.5, 25, 27.5, and 30 Hz were carried out and the displacements recorded by the six lasers were obtained to compute the rotation and the displacements of the center of the tub using Equations (3.7) to (3.36). Since the three rotation angles and the two horizontal

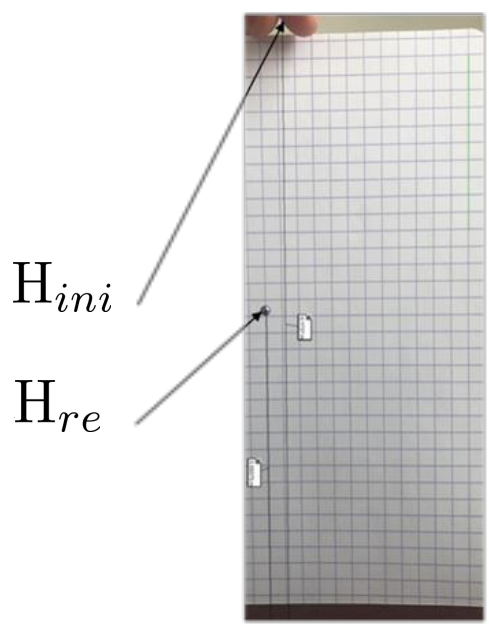

Figure 4.2 Bounce test of a media dropped against the same rubber material as the tub liner. H_{ini} is the height measured at the initial position and H_{re} is the measured height after first rebound. The test was performed with an iPhone X Camera recording at 240 fps. H_{ini} and H_{re} were determined by analyzing the frames with Loggerpro software.

displacements (U_x and U_y) are very small, when compared to the vertical displacement U_z, as shown in Figure 3.7, therefore only the vertical displacement that was computed at the center was imported into the DEM model for simplification. Figure 4.4 presents the vertical displacements U_z of the center of the tub computed for the six frequencies of 17.5, 20, 22.5, 25, 27.5, and 30 Hz during a one second period. It can be seen that, for each of the shaft frequencies, there exist several sub-frequencies, which relate to different modes of vibration. A Fourier analysis of U_z was performed to obtain the actual vibration amplitudes and frequencies for each of the shaft frequencies. Figure 4.4 shows that several sub-frequencies of vibrations with the corresponding amplitudes occur during the vibratory peening process. Figure 4.5 presents the Fourier analysis results of the U_z displacement curves in a 5-minutes recording period for the 6 shaft frequencies of 17.5, 20, 22.5, 25, 27.5, and 30 Hz. Table 4.1 lists the considered amplitudes (A) and frequencies (F) loadings applied in the DEM model to simulate the media movement inside the tub. For the shaft frequencies of 17.5, 20, 25 and 27.5 Hz, only one pair of amplitude and frequency were imported into the DEM model. However, for the shaft frequencies of 22.5 and 30 Hz, a second vibration mode was added. Therefore, two pairs of amplitude and frequency inputs were imported into the DEM simulations. This large amplitude is due to resonant modes of the vibratory peening machine. The aim of this study was to reproduce as close as possible the vertical displacement to the raw measurements of the vertical position in Figure 4.4. A maximum of 2 modes of vibration was set to keep a simple modelling of the displacement of the tub. Figure 4.6 shows that for a time scale of one second, building the signal with 2 modes of vibration for 30 Hz is sufficient. For several minutes of vibration, it may not be relevant to use only 2 modes of vibration since the signal is no longer periodic for long time scales, as shown in Figure 4.3 because the amplitude of vibration varies from 20 mm to 40 mm between 60 seconds and 80 seconds of operation.

Table 4.1 Vibrations modes (amplitude and frequency) at for X_{Freq} values of 17.5, 20, 22.5, 25, 27.5, and 30 Hz resulting from the Fourier analysis.

X_{Freq}	17.5 Hz	20 Hz	22.5 Hz	25 Hz	27.5 Hz	30 Hz
Mode of vibration (amplitude (mm), frequency (Hz))	(2.6,17.7)	(2.1,20.2)	(5.3,3.0) (2.1,22.7)	(2.1,25.2)	(2.3,27.7)	(8.5,3.0) (1.7,30.2)

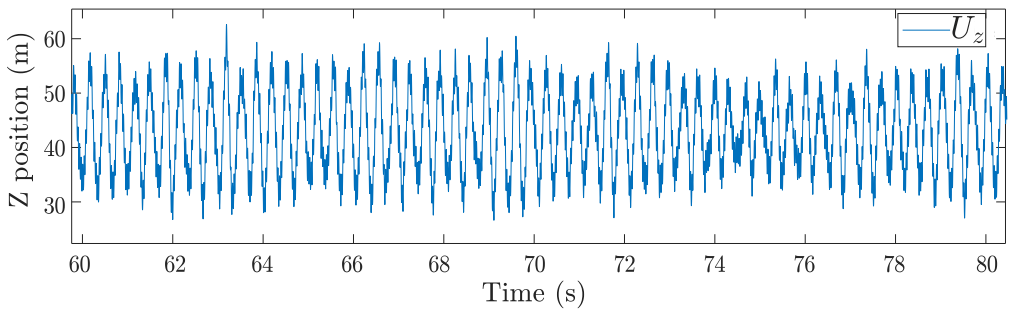

Figure 4.3 Vertical displacement of the tub at 20 Hz during 20 seconds. The amplitude of vibration varies for long time scale so the signal is no longer periodic. So the model of 2 modes of vibration for the vertical motion is relevant for a small period of simulation of 2 seconds or less.

4.2 Comparison of experimentally measured impact velocities with the prediction by the DEM model.

4.2.1 Computation of the velocities from the experiments

The validation of the DEM model was performed by comparing the motion of media on an aluminium block between the DEM simulation and the actual motion. An aluminium block was fixed against the glass observation window on the front side of the vibratory tub, as shown in Figure 4.7. In the simulation, the block is also fixed against a wall to have the same boundary conditions. The impact velocities between the media and the aluminium block in the experiment were obtained by recording the process with an iPhone X camera at a recording rate of 240 fps. The recorded images were analyzed by Loggerpro software through manually tracking one particle. This software allows to associate a particle to a point manually frame by frame. The output of this tracking is a file of the positions of every point that is tracked according to the frames. This allows to compute vertical velocities of particles. The machine parameters were $X_{Freq} = 30$ Hz, $X_{Mass} = 544$ kg, $X_{Ecc} = 24$ kg/shaft, $X_{Press} = 2.8$ bar, $X_{Height} = 150$ mm, X_{Pos} in the middle and $X_{Lub} = 20$ rpm.

4.2.2 Computation of the velocities from the experiments

Figure 4.7 shows the method for measuring the normal impact velocities on the bottom face of the aluminium part with software Loggerpro. Figure 4.8 shows the part and the particle tracked for 2 frames of the video. This tracking is done for a period of 0.17 seconds and the resulting positions of the tracking of the particle and the aluminium block are presented in Figure 4.9. Figure 4.10 represents 3 screenshots of the particles impacting the aluminium

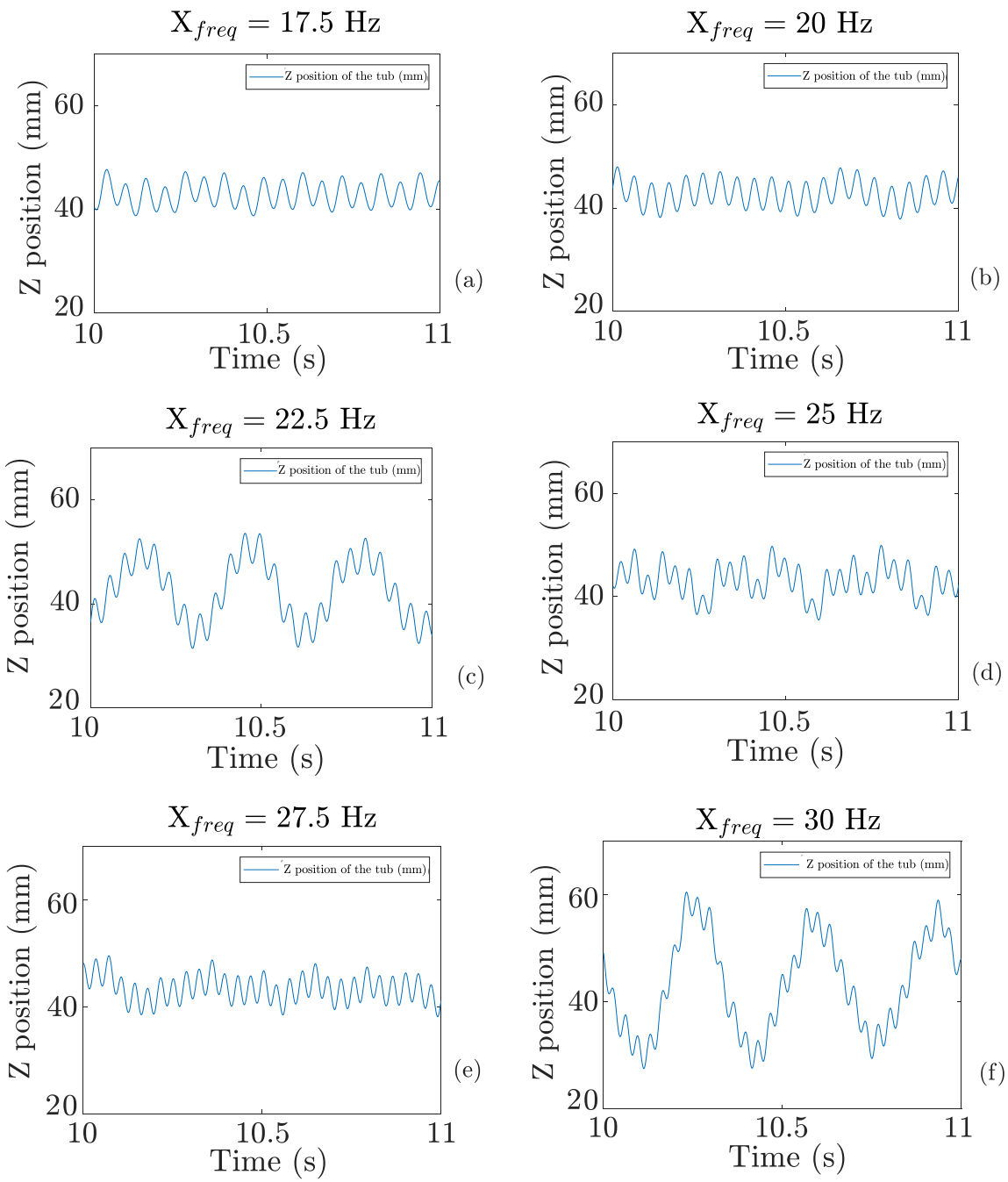

Figure 4.4 Vertical displacements U_z at the center of the tub for six frequencies of (a) X_{Freq} = 17.5 Hz, (b) X_{Freq} = 20 Hz, (c) X_{Freq} = 22.5 Hz, (d) X_{Freq} = 25 Hz, (e) X_{Freq} = 27.5 Hz, and (f) X_{Freq} = 30 Hz during a one second period for the parameters X_{Mass} = 544 kg, X_{Ecc} = 24 kg/shaft, X_{Press} = 2.8 bar, X_{Height} = 150 mm, X_{Pos} in the middle and X_{Lub} = 20 rpm. A low frequency mode of vibration with large amplitude appears for 22.5 Hz and 30 Hz.

block at 0.054 s, 0.108 s and 0.162 s. The amount of red dots represents the particle that is tracked, the amount of blue dots represents the aluminium part that is tracked and the green

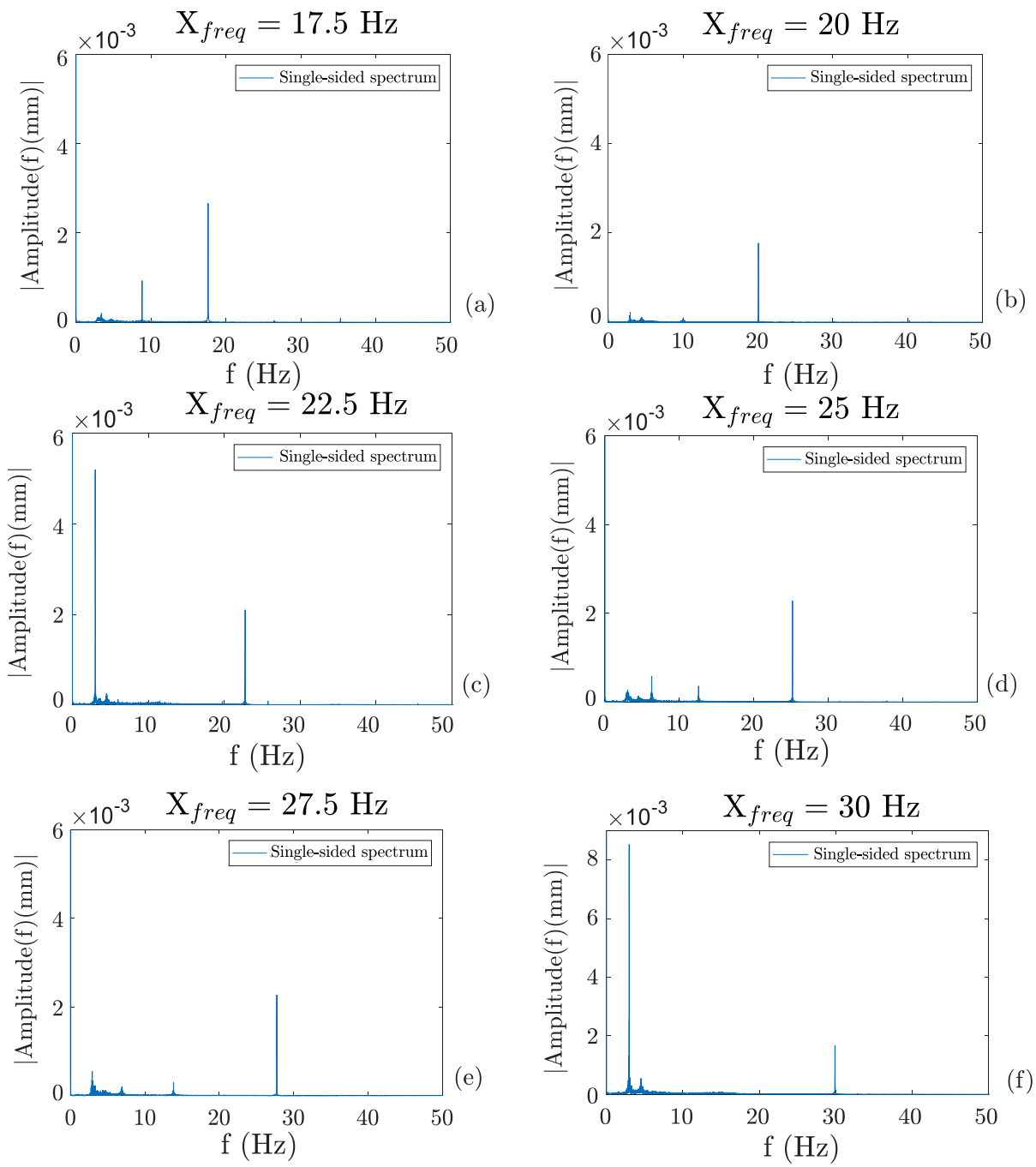

Figure 4.5 Fourier transform of the displacement signals in Figure 19 for six frequencies of (a)X_{Freq} = 17.5 Hz, (b) X_{Freq} = 20 Hz, (c) X_{Freq} = 22.5 Hz, (d) X_{Freq} = 25 Hz, (e) X_{Freq} = 27.5 Hz, and (f) X_{Freq} = 30 Hz during a one second period for the parameters X_{Mass} = 544 kg, X_{Ecc} = 24 kg/shaft, X_{Press} = 2.8 bar, X_{Height} = 150 mm, X_{Pos} in the middle and X_{Lub} = 20 rpm.

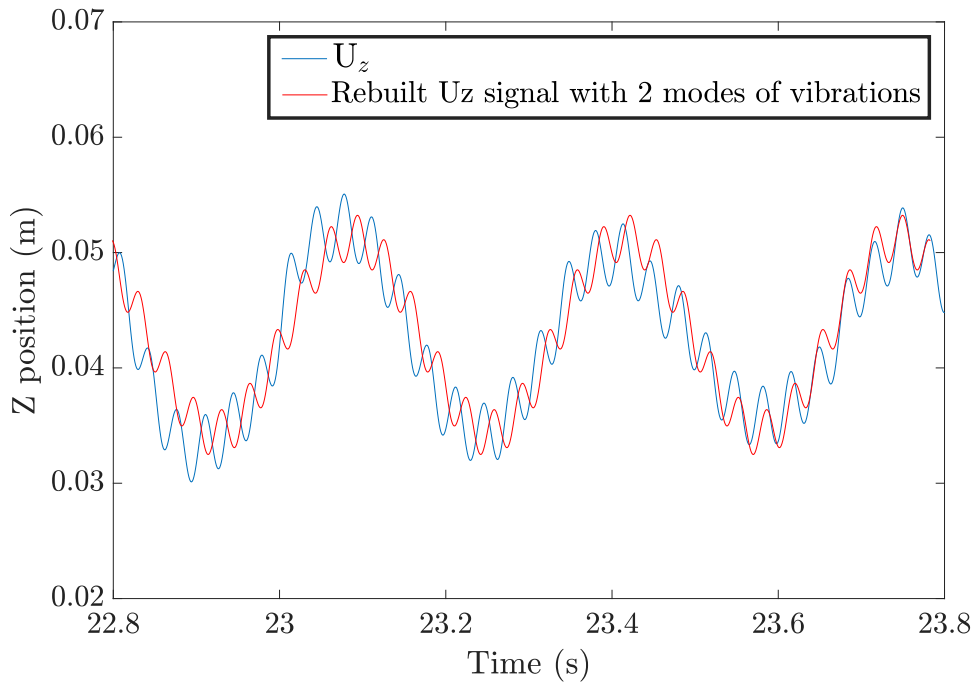

Figure 4.6 Vertical displacement of the machine at 30 Hz. The blue curve is the raw signal of the vertical displacement of the vibratory peening machine at 30 Hz from Figure 4.4 (f) and the red curve is the rebuilt vertical displacement of the vibratory peening machine using two modes of vibration of the Fourier transforms from Figure 4.5 (f). Two modes of vibration are sufficient to build the vertical position of the tub for a small period of time.

line is the reference distance for the computation of the velocity. Figure 4.11 presents the vertical velocities of one particle during the vibratory peening process, which was manually tracked to differentiate its position with respect to time. The normal velocity according to time $V_n(t)$ is computed as follows:

$$V(t) = (Particle(t + dt) - Particle(t)) \times 240, \tag{4.2}$$

with $Particle(t)$ being the position of the tracked particle at time t and $Particle(t+dt)$ being the position of the tracked particle at time $t + dt$ with $dt = 1/240 = 0.00416$ s. Therefore, the relative velocity of the particles to that of the aluminium block is computed as per

$$RV(t) = \frac{P_a(t) - P_m(t)}{\Delta t}, \tag{4.3}$$

where RV is the relative velocity according to time t, P_a is the position of the aluminium block, P_m is the position of one media and $\Delta t = \frac{1}{240} \approx 0.0042$ s. To be even more confident, more particles could be tracked to have a distribution of impact velocities against the

aluminium part.

Three normal impact velocities were measured. The average normal impacting velocity of the media on the aluminium part was 0.89 m/s with standard deviation of 0.08 m/s. The times of impact velocities are determined thanks to the visualization of the impacts as shown Figure 4.10.

4.2.3 Computation of the velocities from the DEM simulations and comparison with the experimentally measured velocities

Two vibration modes (mode 1: A1 = 8.5 mm, F1 = 3.0 Hz and mode 2: A2 = 1.7 mm, F2 = 30 Hz), as listed in Table 4.1, were simulated in the DEM model for a shaft frequency of 30 Hz to simulate the impact between the particles and the aluminium part. Figure 4.12 shows the simulated relative velocity of the media. For 10 simulated impacts, the average normal relative to one media is 0.95 m/s with standard deviation of 0.02 m/s, which is similar to the experimentally measured value of 0.89 m/s with a standard deviation of 0.08 m/s.

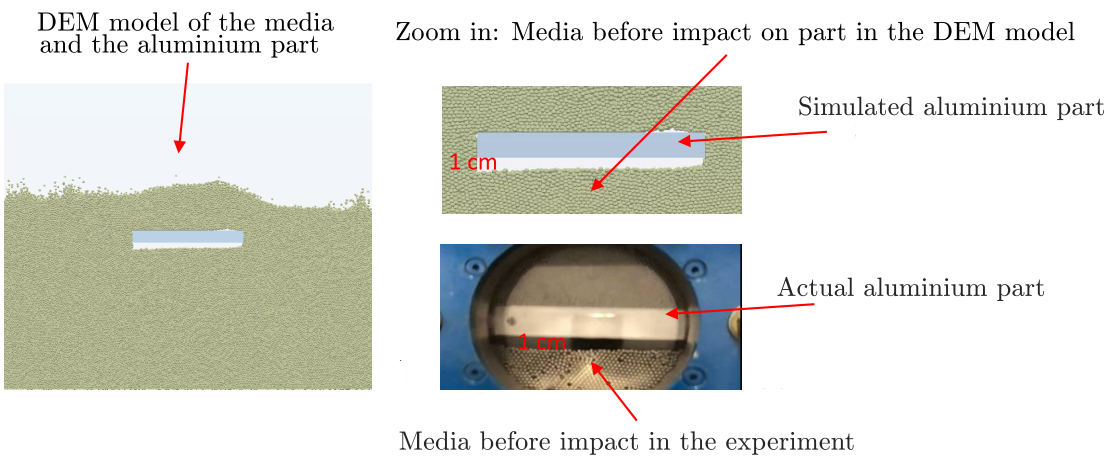

Figure 4.7 Screenshot of media before impact from the DEM model and measurements for a 30 Hz shaft frequency. (a) DEM model with an aluminium block having dimensions of $20 \times 150 \times 20$ mm^3. Two vibration modes (A1 = 8.5 mm, F1 = 3.0 Hz and A2 = 1.7 mm, F2 = 30 Hz) are applied to the tub, whose dimensions are $20 \times 500 \times 500$ mm^3, containing 1.1×10^5 steel particles having a diameter of 3 mm. (b) Zoom in on the DEM model showing the gap between the bottom of the aluminium holder and the media. (c) Visualization of the aluminium block through the window of the tub: $X_{Freq} = 25$ Hz, $X_{Mass} = 544$ kg, $X_{Ecc} = 24$ kg/shaft, $X_{Press} = 2.8$ bar, $X_{Height} = 150$ mm, X_{Pos} in the middle and $X_{Lub} = 20$ rpm. The relative distance under the part is 1 cm for the simulation and experiments.

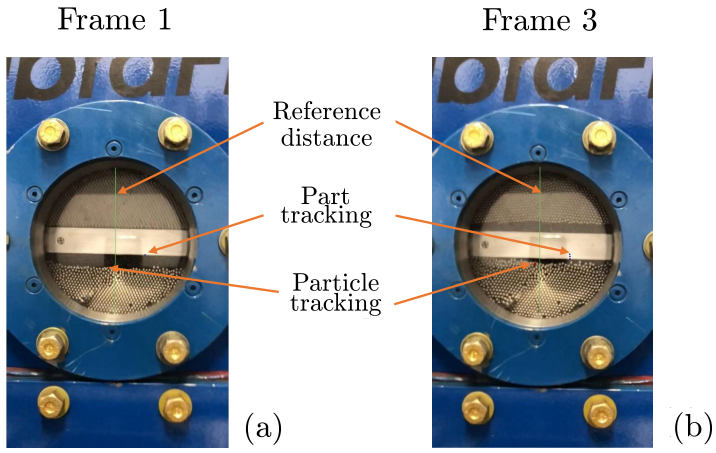

Figure 4.8 Computation of the velocity with Loggerpro from the frames of the video recording. The aluminium part and one particle are manually tracked to get the relative position for every frame of the video, and normal velocity with respect to time. (a) shows the track of one particle and aluminium block at frame 1 and (b) shows the track of one particle and aluminium block at frame 3. The green line represents the reference distance that has physically been measured and is needed to convert a number of pixels into an actual distance, to compute the velocities in m/s.

Although the statistical volume tracked media is quite small, the proposed method was an efficient method to quickly obtain the impact velocities of media against the aluminium part.

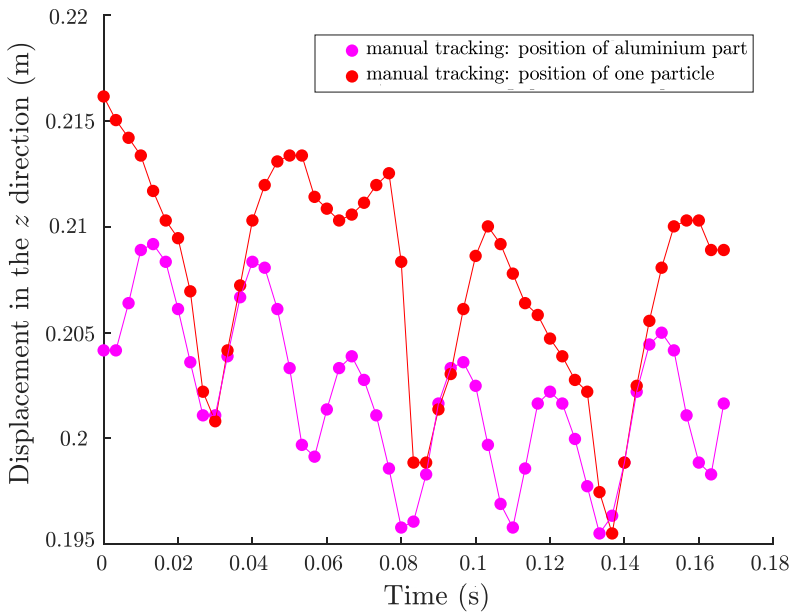

Figure 4.9 Position of the aluminium part and the media are tracked to compute the relative velocity between the aluminium part and media. All the points were tracked manually using the frames of the video recorded by an iPhone X camera at 240 fps analyzed by the software Loggerpro.

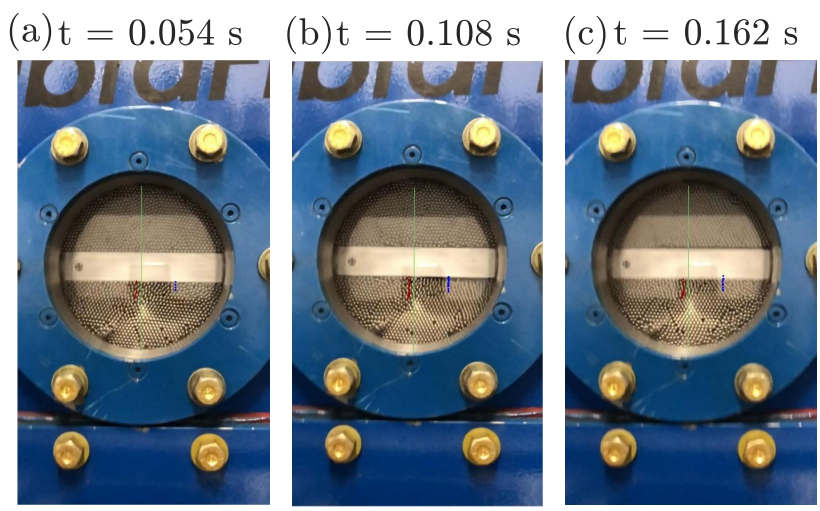

Figure 4.10 Impacts at different time steps for the parameters $X_{Freq} = 30$ Hz, $X_{Mass} = 544$ kg, $X_{Ecc} = 24$ kg/shaft, $X_{Press} = 2.8$ bar, $X_{Height} = 150$ mm, X_{Pos} in the middle and $X_{Lub} = 20$ rpm. This allows to know when each impact occurs. Blue dots and red dots represent the tracking of the aluminium block and one particle, respectively.

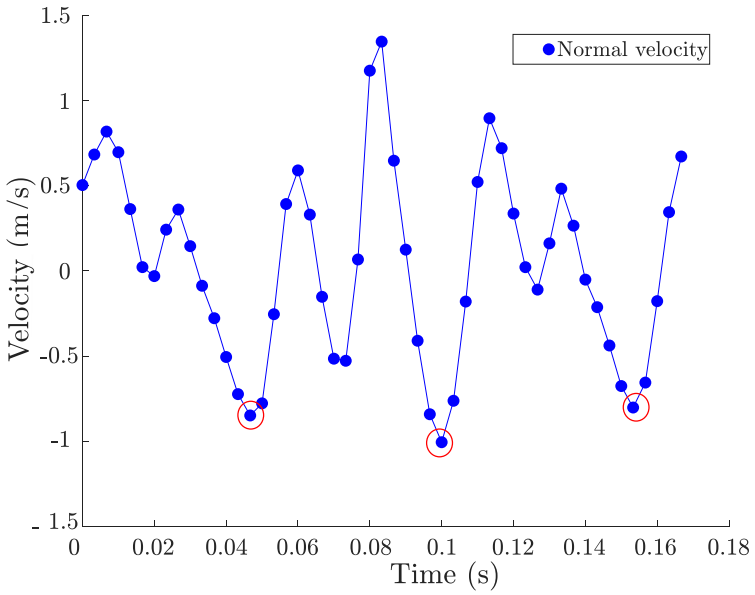

Figure 4.11 Normal velocity of one particle impacting aluminium block for 30 Hz rotating shaft. Red circles represent the impact velocity. The motion is assumed vertical and media is assumed to impact perfectly perpendicularly the aluminium block. Impact velocities are negative because the frame in Logger software points down.

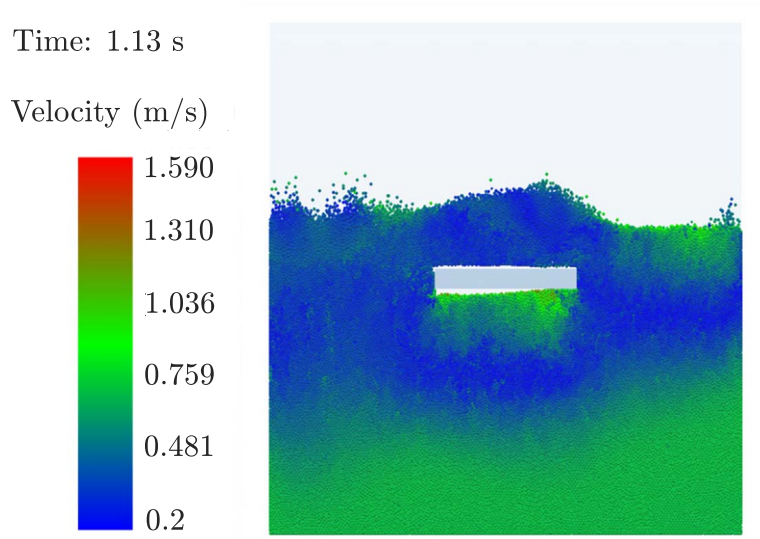

Figure 4.12 Normal absolute velocity of the particles in the DEM validation simulation. The aluminium block had dimensions of $20 \times 150 \times 20$ mm^3. Two vibration modes (A1 = 8.5 mm, F1 = 3.0 Hz and A2 = 1.7 mm, F2 = 30 Hz) and 1.1×10^5 steel particles having a diameter of 3 mm were simulated. Tub dimensions are $20 \times 150 \times 500$ mm^3. The impact velocity field is homogenous under the aluminium part.

This chapter has allowed to create and validate a discrete element model with 1.1×10^5 particles. The coefficient of restitution between the walls and the particles was one of the key parameters to computed the media velocities during operation. The model was validated by measuring particle impacts against an aluminium part and compare it to the simulations.

CHAPTER 5 Correlation between Almen intensity and media velocity

5.1 Approach to understand the process

In this chapter, three studies were performed. The first study is an experimental one that provides experimental data of Almen intensity according to shaft frequency of the VP machine. The second study is a numerical one that allowed to develop a relationship between the shaft frequencies of the VP machine and the impact velocities of the particle against the strip with a DEM model. The third study is an analytical model that comes from the literature and describes the relationship between the Almen intensity and the impact velocity of shot in shot peening.

The first and the second studies were performed to get a combination of experimental and numerical modelling of Almen intensity according to media impact velocities. They were compared to the analytical study that also provided a relationship between experimental Almen intensity and media impact velocities. So the objective is to combine the experimental study and the simulation study that permit to find a relation between impact velocities and Almen intensity and compare this relation with an analytical study that provides the evolution of Almen intensity according to the velocity of a single shot.

5.2 Experimentally measured Almen intensity

Almen saturation curves were performed to obtain the relationship between the resulting Almen intensity with respect to the frequency, as shown in Figure 5.1. A similar linear relationship between Almen intensity and vibratory peening frequency can be observed with a small exception at the frequency of 22.5 Hz, which is similar to the tendency shown in Figure 5.3.

5.3 Simulation of the impact velocity while the machine is operating

Simulations of the media impacting on an Almen strip at the six shaft frequencies were performed. The post-processing, shown in Figure 5.2, shows the predicted media impact velocity at $t = 0.984$ s for 1.1×10^5 particles vibrating at $X_{\text{Freq}} = 27.5$ Hz (A = 2.3 mm, F = 27.7 Hz). Figure 5.3 presents the simulated average normal impact velocities to the Almen strip for six shaft frequencies of 17.5, 20, 22.5, 25, 27.5 and 30 Hz, with a media mass of 544 kg and vibrating for two seconds. In EDEM software, every collision is tracked between

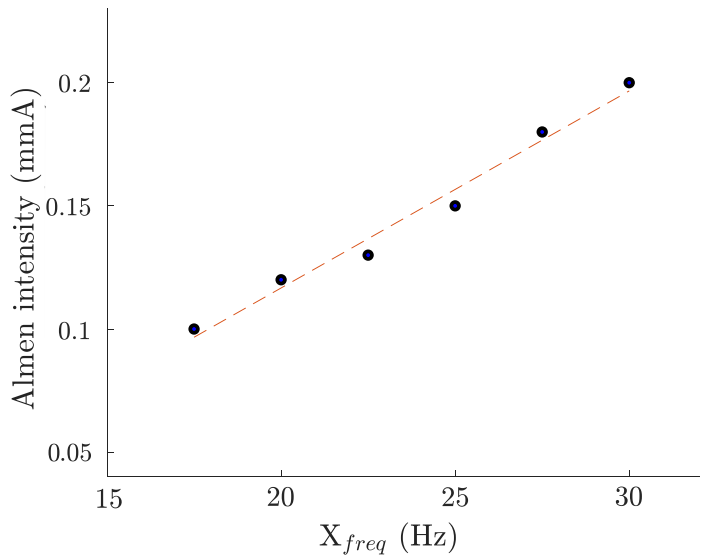

Figure 5.1 Relation between experimentally measured Almen intensity and vibratory peening frequency , $X_{Mass} = 544$ kg, $X_{Ecc} = 24$ kg/shaft, $X_{Press} = 2.8$ bar, $X_{Height} = 150$ mm, X_{Pos} in the middle and $X_{Lub} = 20$ rpm.

all particles and the Almen strip. Every collision is associated to a normal impact velocity so all the impact velocities are saved. The normal impact velocity presented in Figure 5.3 is the average velocity of all the impacts against the Almen strip. It can be seen that there is a linear correlation between velocity and machine frequency.

5.3.1 Comparison of Almen intensity and impacting velocities for VP and SP

Figure 5.4 reports the experimentally measured Almen intensity as a function of the predicted impacting velocity of the media. Figure 5.4 also plots the predicted Almen intensity model by Miao et al. [42]. The figure shows that the range of Almen intensities reached is almost the same for the 6 measurements (0.1 mmA to 0.2 mmA) and conventional shot peening (0.095 mmA to 0.200 mmA), which means that the vibratory peening process can achieve the same Almen intensity range as conventional shot peening.

From both simulations and experiments, an empirical linear correlation between impact velocities and Almen intensity is obtained as:

$$I = 0.2564 \times V - 0.0724, \tag{5.1}$$

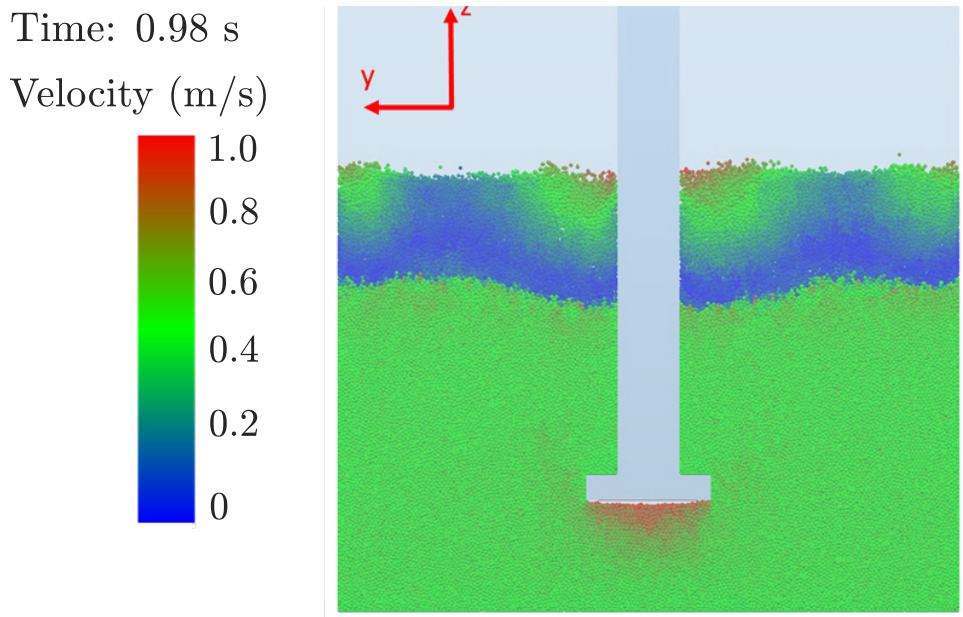

Figure 5.2 Velocity distribution of media for $t = 0.984$ s. The frequency mode is $X_{Freq} =$ 30 Hz (A = 2.3 mm, F = 27.7 Hz). The simulation featured 1.1×10^5 steel particles having a diameter of 3 mm and the tub dimensions were $20 \times 500 \times 500$ mm^3.

where I is the Almen intensity (mmA) and V the normal impact velocity of the particles (m/s). A coefficient of determination $R^2 = 0.999$ was obtained for the experiments & DEM simulation points. In the case of a round steel particle impacting a steel surface, the relation between Almen intensity and impact velocity is also linear as shown in Figure 5.3. From Figure 5.4, it can be seen that larger impact velocities (1.2 m/s to 2.5 m/s) are needed to reach the same Almen intensities as those obtained for lower velocities (0.6 m/s to 0.95 m/s) during vibratory peening. This could partly result from the large mass of the media where not only dynamic impact but also static compression works simultaneously on the Almen strip. Further investigation is required for a deeper understanding of the difference of the two processes.

5.4 Influence of history of the tub on media packing

For every process conditions applied in this study, the initial position of the media is different and depends on the treatment history. Indeed, the packing of the particles at the end of a test after a certain amount of time is not the same for two different modes of vibration. To prove that the history of the tub has an influence on the packing of the particles, three simulations were conducted. For each simulation, the 20 Hz mode is run for 30 seconds, then

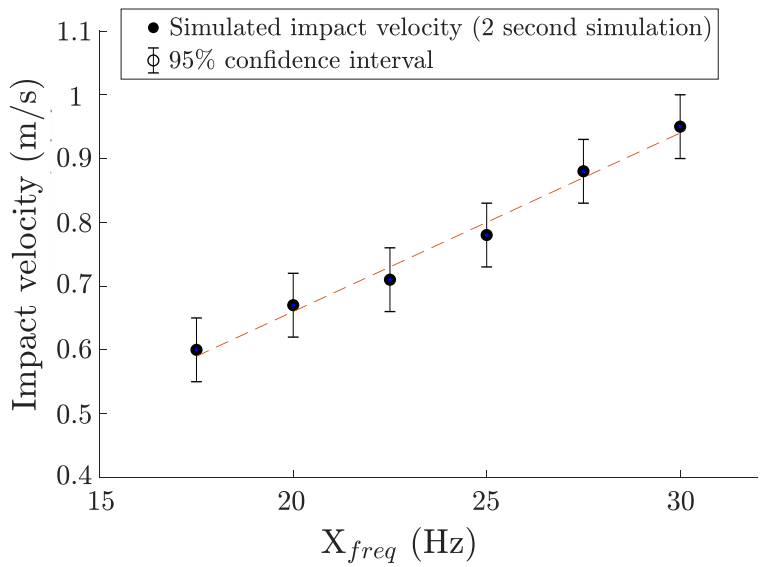

Figure 5.3 DEM simulated impact velocities during 2 seconds as a function of shaft frequencies X_{Freq} , $X_{Mass} = 544$ kg, $X_{Ecc} = 24$ kg/shaft, $X_{Press} = 2.8$ bar, $X_{Height} = 150$ mm, X_{Pos} in the middle and $X_{Lub} = 20$ rpm.

the 30 Hz mode is run for the next 30 seconds, finally the 20 Hz mode is run again for 60 more seconds. The only difference for the three simulations is the initial positions of the particles that is obtained randomly with EDEM. To reduce the computational time, the packing was measured in a small volume, as shown Figure 5.5. Compactness is defined as the fraction of volume occupied by the media.

As shown in Figure 5.6, the packing is not the same: compactness are 0.618 for $X_{freq} = 20$ Hz and 0.626 for $X_{freq} = 30$ Hz. However, when the 20 Hz mode is running after the 30 Hz mode, the packing is 0.626 at 60 s which is different from the value of 0.605 at 0 s. In addition, it can be seen that, from 60 s to 120 s, for the three simulations, the compactness remains larger value of 0.625 than that at 30 s of 0.618. Moreover, the simulations presented in Figure 5.6 have been repeated three times with random packing of particles and it showed that the packing at 30 Hz is 62.5% for the three simulations. Therefore, it suggests that running the machine at 30 Hz generates the same packing of media since it is the highest possible packing. Notice that the compactness has not been computed for the frequencies of 17.5 Hz, 20 Hz, 22.5 Hz, 25 Hz and 27.5 Hz. This is a suggestion as a future work to verify that 30 Hz generates the highest compactness in the tub.

These simulations showed repeatable results and proved that the previous treatment done by the VP machine has an impact on the packing of media for the next treatment. The 30 Hz shaft frequency induces the most compact media packing in less than 30 seconds. So

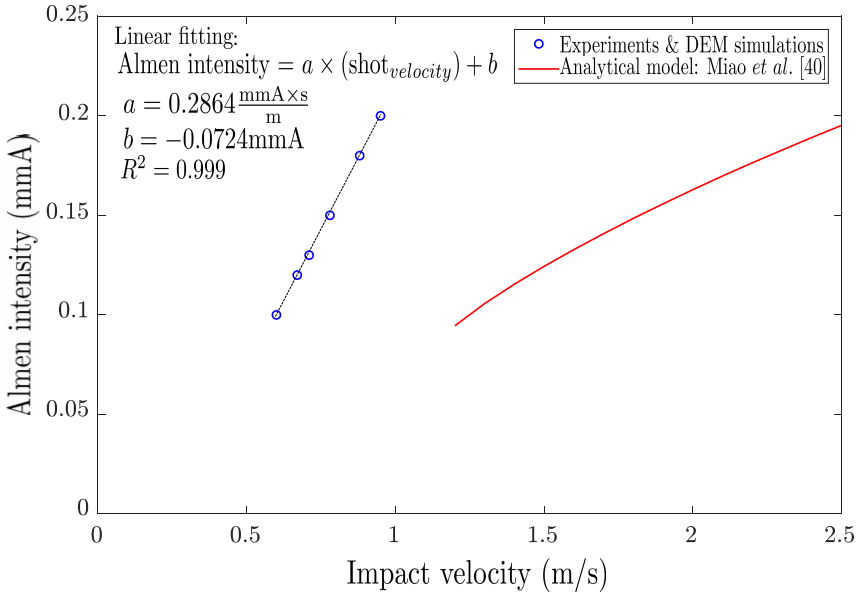

Figure 5.4 Experimental Almen intensity vs simulated impact velocity from EDEM simulations and from the model of [42]. The blue circles represent the experimentally measured Almen intensity during VP according to the corresponding impact velocities from the DEM model. The red curve represents the analytical model of Almen instensity produced by a steel shot against an Almen strip according to the shot impact velocity. A linear relationship is found for VP peening as for the analytical model of [42]. The velocity range is lower for VP than SP due to inertia effect of several layers of particles impacting the workpiece.

to have repeatable results experimentally, imposing a vibration mode of 30 Hz before every treatment allows to have the same initial packing.

This chapter has shown with DEM simulations that the impact velocity of media against the Almen strip is linear with the Almen intensity. Moreover, the packing of the media can be computed with the DEM method so it provides even more information that are useful for leading the experiments.

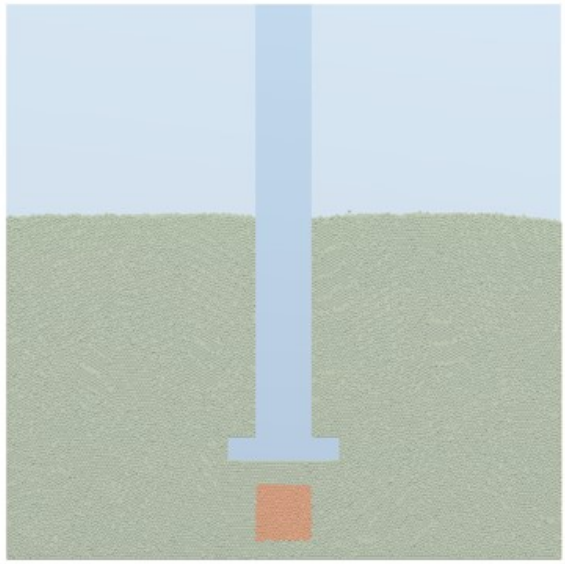

Figure 5.5 Volume (orange square) in which compactness is computed with EDEM during the three simulations contains between 8563 and 8820 particles according to the timestep of simulations.

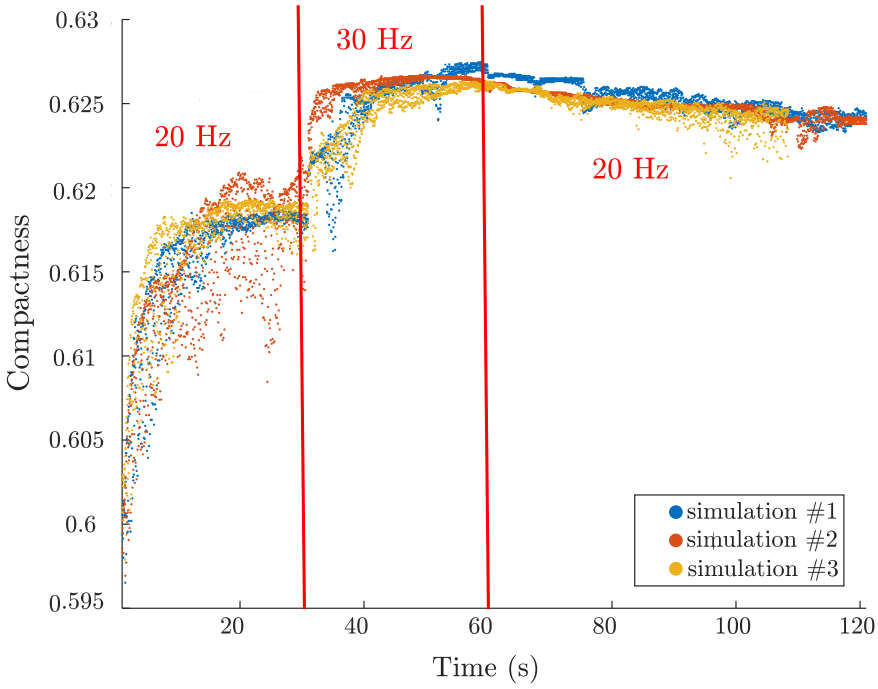

Figure 5.6 Compactness of media under the strip for 120 s for two different values of X_{freq} = 20 Hz from 0 s to 30 s and from 60 s to 120 s, and X_{freq} of 30 Hz from 30 s to 60 s. The 30 Hz mode induces the most compact media packing.

CHAPTER 6 Conclusion and future work

6.1 Conclusion

A setup of six laser sensors was installed to compute the movement of the vibratory peening machine by computing its rotations and displacements. The experimental analysis of motion with laser sensors showed that the vertical displacement prevails over the other displacements and rotations, which was expected from what was found in the literature review about the vibratory peening machines. Therefore, the vertical displacement recorded by the laser sensors were treated by FFT and the (frequency, amplitude) pairs were imported into a DEM model to simulate the movement of the vibratory peening machine. The FFT also revealed that the shaft frequency studies of 22.5 Hz and 30 Hz induced two main modes of vibrations while applying the treatment frequencies of 17.5 Hz, 20 Hz, 25 Hz and 27.5 Hz showed that one main frequency mode was induced, which was corresponding to the shaft frequency. This result was unexpected since the multiple modes of vibrations are not mentioned in the literature review. The reduced size of the numerical model of the vibratory peening machine with dimensions of $500 \times 20 \times 500$ mm^3 and 1.1×10^5 steel particles having a diameter of 3 mm was developed to represent the real vibratory tub. The parameters of the numerical model were determined experimentally such as the restitution coefficient between the media and the tub. The kinematics parameters of the model were the main modes of vibrations that have been measured, which is a limitation of the simulations because the raw signal was not used as input. This is not a significant issue for our simulation because the constructed signal using the Fourier transforms is close to the raw signal for small amounts of times such as 2 seconds. If the vertical motion was not periodic, the raw signals of the motion should have been used.

This work led to the main conclusions listed as follows:

- The instrumentation of the machine with laser sensors was proven to be robust and an efficient way on measuring the machine's movement.

- The particles' displacement fields and velocity fields were computed to determine the normal impact velocity of media against a steel strip. The DEM model was validated by comparing the amplitude of displacement of particles for both numerical and experimental data.

- In the end, the comparison of the simulated impact velocities of media on the strip and the experimental Almen intensity has provided a linear correlation for the vibratory peening

conditions with $X_{Freq} = [17.5, 20, 22.5, 25, 27.5, 30$ Hz], $X_{Mass} = 544$ kg, $X_{Ecc} = 24$ kg/shaft, $X_{Press} = 2.8$ bar, $X_{Height} = 150$ mm, X_{Pos} in the middle and $X_{Lub} = 20$ rpm. This validates the model because the linear relationship was expected from the litterature, with a lower range of impact velocities due to the inertia effect of all particles for VP.

- The behavior of the media was also studied and simulations have shown that the history of the tub has an effect on the stacking of the particle, which means that media stacking depends on the previous frequencies of the machine.

Those simulations have permitted to create an empirical law between shaft frequencies and Almen intensity so this allows to master the intensity that needs to be reached by choosing the frequency of the vibratory peening machine. The limitation is that this conclusion is only valid for specific machine parameters of $X_{Mass} = 544$ kg, $X_{Ecc} = 24$ kg/shaft, $X_{Press} = 2.8$ bar, $X_{Height} = 150$ mm, X_{Pos} in the middle and $X_{Lub} = 20$ rpm. Therefore, I believe that it cannot directly be extrapolated to other machine parameters directly. Nevertheless, it provides a window of operation in which the Almen intensity can be predicted.

A study on the media behavior has permitted to show that 20 Hz and 30 Hz modes of vibrations had a different effect on the media stacking. A 20 Hz mode of vibration induces an average compactness of 0.617 while a 30 Hz mode of vibration induces an average compactness of 0.627. Moreover, treating at 20 Hz after a 30 Hz treatment does not change the stacking of the media. This could have an impact on the repeatability of the process. The stacking of media according to the vibratory peening frequency was never studied before. This might be a key to understand whether the vibratory peening process can always be repeatable or not. But one question still remains: how can compactness be experimentally measured inside the tub. More simulations should be performed at more frequencies to measure the compactness of media under the strip. To validate that the order of frequencies in the treatment has an impact on Almen intensity, experimental treatments should be run at three frequencies while simulations are to be performed with the same machine parameters to get the impact velocities against the Almen strip. For the moment, to have a more repeatable process, it is suggested to run the vibratory machine for 30 seconds at 30 Hz to ensure the same initial state of media for every treatment.

These DEM studies are limited by the limited size of the modelled tub. Moreover, this study is very specific on the vibratory peening machine in this study. For instance, the geometry of the holder, the workpiece and the tub are not the same for each vibratory peening machine so the velocity fields that were obtained cannot be generalized for each vibratory peening machine. The discrete element model validation is also limited because it can only validate

the model at the edge of the tub using the window on the VP machine, media velocity fields near the workpiece during operation could not be experimentally measured.

6.2 Future work

• For further analysis of the process, other simulations should be performed by changing parameters X_{Height}, X_{Mass} and X_{Pos} to have a more global understanding of the process and to validate the linear correlation between Almen intensity and simulated normal impact velocity on the strip. Also, longer simulations should be performed with the raw measurements of the tub to get closer to the physical model. Also, a sensitivity study should be performed to show the effect of parasite movement of the machine on the impact velocities that are simulated. A model at the physical scale could also be done to demonstrate that reducing the scale for the model presented was relevant. Moreover, some impacts should be modelled in a DEM-FEM coupled model using several layer of particles to have a superior understanding of the transmitted energy and therefore the resulting Almen intensity.

• The lubrication effect was not modelled in this project. So a coupled CFD-DEM model taking lubrication into account would be a real asset to study the effect of the impact velocity of media shots against the workpiece.

• For further industrialization of the process, it is suggested to use the laser set up presented in this research to find the modes of vibrations that are repeatable. Also, to have a more repeatable process, it encouraged to run the vibratory machine without workpiece for 30 seconds at 30 Hz to keep as much as possible the same initial state of media before every treatment.

REFERENCES

[1] T. Klotz *et al.*, "Surface characteristics and fatigue behavior of shot peened Inconel 718," *International Journal of Fatigue*, vol. 110, pp. 10–21, 2018.

[2] D. E. Semones and W. H. Safranek, "Chemically accelerated metal finishing process," Sep. 14 1976, uS Patent 3,979,858.

[3] F. Hashimoto, S. P. Johnson, and R. G. Chaudhari, "Modeling of material removal mechanism in vibratory finishing process," *CIRP Annals*, vol. 65, no. 1, pp. 325–328, 2016.

[4] J. Solis Romero, A. Anguiano García, and A. García Macedo, "Surface roughness and residual stresses on the fatigue life of shot peened components: Theoretical determination," *Ingeniería mecánica, tecnología y desarrollo*, vol. 3, no. 1, pp. 17–20, 2008.

[5] S. Gangaraj and G. Farrahi, "Side effects of shot peening on fatigue crack initiation life," 2011.

[6] A. Inoue, T. Sekigawa, and K. Oguri, "Fatigue property enhancement by fine particle shot peening for aircraft aluminum parts," in *Conf Proc: ICSP-10, Tokyo, Japan*, 2008.

[7] L. Canals *et al.*, "Effect of vibratory peening on the sub-surface layer of aerospace materials Ti-6Al-4V and E-16NiCrMo13," *Journal of Materials Processing Technology*, vol. 264, pp. 91–106, 2019.

[8] A. Gariépy *et al.*, "On the effect of the peening trajectory in shot peen forming," *Finite Elements in Analysis and Design*, vol. 69, pp. 48–61, 2013.

[9] T. Hong, J. Ooi, and B. Shaw, "A numerical simulation to relate the shot peening parameters to the induced residual stresses," *Engineering Failure Analysis*, vol. 15, no. 8, pp. 1097–1110, 2008.

[10] S. Meguid, G. Shagal, and J. Stranart, "Finite element modelling of shot-peening residual stresses," *Journal of Materials Processing Technology*, vol. 92, pp. 401–404, 1999.

[11] A. Yabuki, M. Baghbanan, and J. Spelt, "Contact forces and mechanisms in a vibratory finisher," *Wear*, vol. 252, no. 7-8, pp. 635–643, 2002.

[12] D. Bańkowski and S. Spadło, "Investigations of influence of vibration smoothing conditions of geometrical structure on machined surfaces," in *IOP Conference Series: Materials Science and Engineering*, vol. 179, no. 1. IOP Publishing, 2017, p. 012002.

[13] S. E. Naeini and J. Spelt, "Two-dimensional discrete element modeling of a spherical steel media in a vibrating bed," *Powder Technology*, vol. 195, no. 2, pp. 83–90, 2009.

[14] K. Hashemnia and J. K. Spelt, "Finite element continuum modeling of vibrationally-fluidized granular flows," *Chemical Engineering Science*, vol. 129, pp. 91–105, 2015.

[15] K. Hashemnia, A. Mohajerani, and J. K. Spelt, "Development of a laser displacement probe to measure particle impact velocities in vibrationally fluidized granular flows," *Powder technology*, vol. 235, pp. 940–952, 2013.

[16] R. Mediratta, K. Ahluwalia, and S. Yeo, "State-of-the-art on vibratory finishing in the aviation industry: an industrial and academic perspective," *The International Journal of Advanced Manufacturing Technology*, vol. 85, no. 1, pp. 415–429, 2016.

[17] M. D. Sangid, J. A. Stori, and P. M. Ferriera, "Process characterization of vibrostrengthening and application to fatigue enhancement of aluminum aerospace components—part I. experimental study of process parameters," *The International Journal of Advanced Manufacturing Technology*, vol. 53, no. 5, pp. 545–560, 2011.

[18] M. D. Sangid, J. A. Stori, and P. M. Ferriera, "Process characterization of vibrostrengthening and application to fatigue enhancement of aluminum aerospace components—part II: Process visualization and modeling," *The International Journal of Advanced Manufacturing Technology*, vol. 53, no. 5, pp. 561–575, 2011.

[19] D. H. Gane *et al.*, "Evaluation of vibrostrengthening for fatigue enhancement of titanium structural components on commercial aircraft," in *Ti-2003 Science and Technology, Proceedings of the 10th World Conference on Titanium, Hamburg, Germany*, 2003, pp. 1053–1058.

[20] G. Feldmann *et al.*, "Application of vibropeening on aero–engine component," *Procedia CIRP*, vol. 13, pp. 423–428, 2014.

[21] W.-F. Wang, "Effect of mns powder additions and vibratory ball peening on corrosion resistance of sintered 316LSC stainless steels," *Powder metallurgy*, vol. 48, no. 2, pp. 151–155, 2005.

[22] D. Ciampini, M. Papini, and J. Spelt, "Characterization of vibratory finishing using the almen system," *Wear*, vol. 264, no. 7-8, pp. 671–678, 2008.

[23] D. Ciampini, M. Papini, and J. Spelt, "Modeling the development of almen strip curvature in vibratory finishing," *journal of materials processing technology*, vol. 209, no. 6, pp. 2923–2939, 2009.

[24] H. Miao *et al.*, "Comparison between vibratory peening and shot peening processes," in *Internatiol Conf. Shot Peen*, 2017, pp. 521–526.

[25] F. Hashimoto and S. P. Johnson, "Modeling of vibratory finishing machines," *CIRP Annals*, vol. 64, no. 1, pp. 345–348, 2015.

[26] Z. Ghemari, "Progression of the vibratory analysis technique by improving the piezoelectric sensor measurement accuracy," *Microwave and Optical Technology Letters*, vol. 60, no. 12, pp. 2972–2977, 2018.

[27] J. Liu and X. Yang, "Artificial neural network for vibration frequency measurement using kinect v2," *Shock and Vibration*, vol. 2019, 2019.

[28] Z. Wu *et al.*, "Three-dimensional reconstruction-based vibration measurement of bridge model using uavs," *Applied Sciences*, vol. 11, no. 11, p. 5111, 2021.

[29] K. Reda and Y. Yan, "Vibration measurement of an unbalanced metallic shaft using electrostatic sensors," *IEEE Transactions on Instrumentation and Measurement*, vol. 68, no. 5, pp. 1467–1476, 2018.

[30] F. Radjai, "The contact dynamics (CD) method," *ALERT Doctoral School 2017 Discrete Element Modeling*, p. 43, 2017.

[31] C. Coetzee, "A johnson-kendall-roberts (JKR) contact model," 2020.

[32] C. Martin, "Advanced contact laws," *ALERT Doctoral School 2017 Discrete Element Modeling*, p. 89, 2017.

[33] J. Y. Alcaraz II *et al.*, "Numerical modeling of residual stresses during vibratory peening of a 3-stage blisk–a multi-scale discrete element and finite element approach," *Journal of Materials Processing Technology*, vol. 299, p. 117383, 2022.

[34] S. Naeini and J. Spelt, "Development of single-cell bulk circulation in granular media in a vibrating bed," *Powder technology*, vol. 211, no. 1, pp. 176–186, 2011.

[35] H. Sakaguchi, E. Ozaki, and T. Igarashi, "Plugging of the flow of granular materials during the discharge from a silo," *International Journal of Modern Physics B*, vol. 7, no. 09n10, pp. 1949–1963, 1993.

[36] B. Blais *et al.*, "Experimental methods in chemical engineering: Discrete element method—dem," *The Canadian Journal of Chemical Engineering*, vol. 97, no. 7, pp. 1964–1973, 2019.

[37] K. Giannis *et al.*, "Stress based multi-contact model for discrete-element simulations," *Granular Matter*, vol. 23, no. 2, pp. 1–14, 2021.

[38] Q. Zheng and A. Yu, "Modelling the granular flow in a rotating drum by the eulerian finite element method," *Powder technology*, vol. 286, pp. 361–370, 2015.

[39] J.-N. Brunet, "Analyse des méthodes par éléments finis et méthodes sans maillage pour la déformation de corps mous en simulation chirurgicale," Ph.D. dissertation, Ecole Polytechnique, Montreal (Canada), 2017.

[40] A. Vijayan, B. Joy, and R. K. Annabattula, "Fluid flow assisted mixing of binary granular beds using CFD-DEM," *Powder Technology*, vol. 383, pp. 183–197, 2021.

[41] L. F. A. Lecornu, *Dynamique appliquée*. O. Doin, 1908, vol. 5.

[42] H. Miao *et al.*, "An analytical approach to relate shot peening parameters to almen intensity," *Surface and Coatings Technology*, vol. 205, no. 7, pp. 2055–2066, 2010.